OPEN ACCESS



Ejecta Masses in Type Ia Supernovae—Implications for the Progenitor and the Explosion Scenario*

```
Zsófia Bora<sup>1,2</sup>, Réka Könyves-Tóth<sup>1,3</sup>, József Vinkó<sup>1,2,3,4</sup>, Dominik Bánhidi<sup>5</sup>, Imre Barna Bíró<sup>5,6</sup>, K. Azalee Bostroem<sup>7,19</sup>, Attila Bódi<sup>1</sup>, Jamison Burke<sup>8</sup>, István Csányi<sup>5</sup>, Borbála Cseh<sup>1,9</sup>, Joseph Farah<sup>8,10</sup>, Alexei V. Filippenko<sup>11</sup>, Tibor Hegedüs<sup>5</sup>, Daichi Hiramatsu<sup>12,13</sup>, Ágoston Horti-Dávid<sup>1,2</sup>, D. Andrew Howell<sup>8,10</sup>,
 Saurabh W. Jha<sup>14</sup>, Csilla Kalup<sup>1,2</sup>, Máté Krezinger<sup>1,2</sup>, Levente Kriskovics<sup>1</sup>, Curtis McCully<sup>8</sup>, Megan Newsome<sup>8,10</sup>, András Ordasi<sup>1</sup>, Estefania Padilla Gonzalez<sup>8,10</sup>, András Pál<sup>1</sup>, Craig Pellegrino<sup>8,10</sup>, Bálint Seli<sup>1,2</sup>, Ádám Sódor<sup>1</sup>,
Zsófia Marianna Szabó<sup>1,15,16</sup>, Olivér Norton Szabó<sup>1,2</sup>, Róbert Szakáts<sup>1</sup>, Tamás Szalai<sup>3</sup>, Péter Székely<sup>3</sup>, Giacomo Terreran<sup>8</sup>,
                                     Vázsony Varga<sup>1,2</sup>, Krisztián Vida<sup>1</sup>, Xiaofeng Wang<sup>17,18</sup>, and J. Craig Wheeler<sup>4</sup>
                        <sup>1</sup> HUN-REN CSFK Konkoly Observatory, Konkoly Thege M. út 15-17, Budapest, 1121, Hungary; bora.zsofia@csfk.hun-ren.hu
                            ELTE Eötvös Loránd University, Institute of Physics and Astronomy, Pázmány Péter sétány IA, Budapest 1117, Hungary
                            <sup>3</sup> Department of Experimental Physics, Institute of Physics, University of Szeged, Dóm tér 9, Szeged, 6720, Hungary <sup>4</sup> Department of Astronomy, University of Texas at Austin, 2515 Speedway, Stop C1400, Austin, TX 78712-1205, USA
                                             Baja Astronomical Observatory of University of Szeged, Szegedi út, Kt. 766, 6500 Baja, Hungary
                                                 ELKH-SZTE Stellar Astrophysics Research Group, Szegedi út, Kt. 766, 6500 Baja, Hungary
                                       <sup>7</sup> Steward Observatory, University of Arizona, 933 North Cherry Avenue, Tucson, AZ 85721-0065, USA
                                                   Las Cumbres Observatory, 6740 Cortona Drive, Suite 102, Goleta, CA 93117-5575, USA
                                                             MTA-ELTE Lendület "Momentum" Milky Way Research Group, Hungary
                                                   <sup>10</sup> Department of Physics, University of California, Santa Barbara, CA 93106-9530, USA
                                      Department of Physics, University of California, Saina Balvala, CA 94700-3530, Contain Department of Astronomy, University of California, Berkeley, CA 94720-3411, USA

12 Center for Astrophysics, Harvard & Smithsonian, 60 Garden Street, Cambridge, MA 02138-1516, USA

13 The NSF AI Institute for Artificial Intelligence and Fundamental Interactions, USA
              <sup>14</sup> Department of Physics and Astronomy, Rutgers, the State University of New Jersey, 136 Frelinghuysen Road, Piscataway, NJ 08854, USA
    15 Scottish Universities Physics Alliance (SUPA), School of Physics and Astronomy, University of St Andrews, North Haugh, St Andrews, KY16 9SS, UK
                                                       Max-Planck-Institut für Radioastronomie, Auf dem Hügel 69, 53121 Bonn, Germany
                       <sup>17</sup> Physics Department and Tsinghua Center for Astrophysics (THCA), Tsinghua University, Beijing, People's Republic of China
                                        <sup>8</sup> Beijing Planetarium, Beijing Academy of Science and Technology, Beijing, People's Republic of China
                                                         Received 2024 May 22; accepted 2024 August 11; published 2024 September 3
```

Abstract

The progenitor system(s) as well as the explosion mechanism(s) of thermonuclear (Type Ia) supernovae are long-standing issues in astrophysics. Here we present ejecta masses and other physical parameters for 28 recent Type Ia supernovae inferred from multiband photometric and optical spectroscopic data. Our results confirm that the majority of SNe Ia show *observable* ejecta masses below the Chandrasekhar-limit (having a mean $M_{\rm ej}\approx 1.1\pm 0.3\,M_{\odot}$), consistent with the predictions of recent sub- $M_{\rm Ch}$ explosion models. They are compatible with models assuming either single- or double-degenerate progenitor configurations. We also recover a sub-sample of supernovae within $1.2\,M_{\odot} < M_{\rm ej} < 1.5\,M_{\odot}$ that are consistent with near-Chandrasekhar explosions. Taking into account the uncertainties of the inferred ejecta masses, about half of our SNe are compatible with both explosion models. We compare our results with those in previous studies, and discuss the caveats and concerns regarding the applied methodology.

Unified Astronomy Thesaurus concepts: Type Ia supernovae (1728); Explosive nucleosynthesis (503); Radiative transfer (1335)

Original content from this work may be used under the terms of the Creative Commons Attribution 3.0 licence. Any further distribution of this work must maintain attribution to the author(s) and the title of the work, journal citation and DOI.

1. Introduction

Both the progenitor configuration and the explosion mechanism of thermonuclear supernovae (Type Ia SNe) are still heavily debated, despite the intense and extensive studies that such events have received for 50+ yr (see. e.g., Maoz et al. 2014; Branch & Wheeler 2017; Livio & Mazzali 2018, for reviews). It has been recognized decades ago that SNe Ia are produced by thermonuclear explosions of carbon–oxygen white dwarfs (C/O WDs). It is also known that the WD must

^{*} Based in part on observations obtained with the Hobby-Eberly Telescope (HET), which is a joint project of the University of Texas at Austin, the Pennsylvania State University, Ludwig-Maximillians-Universitaet Muenchen, and Georg-August Universitaet Goettingen. The HET is named in honor of its principal benefactors, William P. Hobby and Robert E. Eberly.

19 LSST-DA Catalyst Fellow.

be in a binary system to be able to reach the physical state that leads to explosion. There are, however, many possible configurations for such a binary system (see, e.g., Figure 2 in Liu et al. 2023). They are usually categorized by the number of WDs in the system: a single-degenerate (SD) configuration contains only one WD, while double-degenerate (DD) systems consist of two WDs (Livio & Mazzali 2018). In addition, the core-degenerate scenario was also proposed (Livio & Riess 2003), in which the WD and the degenerate core of an AGB star rapidly merge during a common-envelope phase. Merging also plays a key role in the DD scenario, although an interesting possibility of a direct WD-WD collision induced by a third body was also considered as an alternative scenario (Thompson 2011). A detailed review of the pros and cons of all these possible progenitor configurations can be found in, e.g., Livio & Mazzali (2018). For further discussion, including a detailed list of references, we refer to Liu et al. (2023).

There are also several possibilities for the explosion mechanism. The key parameter is the mass of the exploding WD, i.e., whether it is close to the Chandrasekhar mass or significantly below it (near-Chandra, or sub-Chandra models, respectively). Liu et al. (2023) gives a detailed summary of the relevant explosion mechanisms, see their Figure 3 and Table 2.

The high degree of homogeneity of the observables of SNe Ia, including light curves (LCs) and spectra, can be explained relatively easily by having $\sim\!\!0.5~M_\odot$ of $^{56}\rm Ni$ surrounded by a layer consisting of mostly $^{28}\rm Si,~^{12}C$ and $^{16}\rm O$ and expanding homologously with $\nu_{max}\approx20,000~km~s^{-1}$ (e.g., Hoeflich 2017). Such an ejecta configuration can be produced by a variety of progenitor systems and explosion mechanisms, involving WDs having either near-Chandra or sub-Chandra masses. Historically, SNe Ia have been thought to arise from the explosion of near-Chandra WDs for many decades. More recent studies found, however, that ejecta masses derived directly from photometric observations (Scalzo et al. 2014a, 2014b, 2019; Könyves-Tóth et al. 2020) resulted in a significant fraction of sub-Chandra masses, which actually turned out to be more numerous than near-Chandra events among the normal SNe Ia (excluding 91T-like and super-Chandra SNe).

Nebular spectroscopy is another powerful tool for constraining ejecta masses. Recent analyses of SNe Ia nebular spectra, both in the optical and near-infrared, compared the observed strength of (forbidden) emission lines of iron peak elements (mostly Ni and Fe) with the theoretical predictions to reveal the possible progenitor systems and explosion types. These studies suggested a mixed population of sub-Chandra and near-Chandra progenitors for the observed events. For example, Maguire et al. (2018), Diamond et al. (2018) and Dhawan et al. (2018) found consistency with near-Chandra delayed-detonation models, while Flörs et al. (2018, 2020) preferred mostly sub-Chandra explosions. Most recently, Liu et al. (2023b) found that ~67% of their sample (24 out of 36 SNe) is consistent with sub-Chandra explosion models.

On the other hand, to explain the ionization balance in late-time SN Ia spectra, the presence of neutron-rich Fe-group elements (like ^{55}Mn and $^{57}\text{Fe},\,^{58}\text{Ni}$) is needed (e.g., Livio & Mazzali 2018). The production of such species and their corresponding decay chains ($^{57}\text{Ni} \rightarrow ^{57}\text{Co} \rightarrow ^{57}\text{Fe},\,\text{or}\,^{55}\text{Co} \rightarrow ^{55}\text{Fe} \rightarrow ^{55}\text{Mn}$) require high central densities, i.e., near-Chandra masses for the exploding WDs (e.g., Seitenzahl et al. 2013). However, this does not rule out sub-Chandra explosions, because those are also capable of producing (at least some fraction of) such neutron-rich isotopes (see, e.g., Shen et al. 2018).

There are also other theoretical arguments that favor near-Chandra, or even super-Chandra WDs at the moment of explosion. In the SD scenario the accreting WD must gain angular momentum as well, resulting in a rapidly spinning, highly magnetized object. Such a WD may significantly exceed the Chandrasekhar mass due to centrifugal forces and magnetic pressure. It must lose its angular momentum in order to reach central density of $\sim 3 \times 10^9 \, \mathrm{g \, cm^{-3}}$ to explode. Such spin-up/spin-down models might explain the existence of Ia-like super-Chandra explosions, but it is uncertain what fraction of the near-Chandra events they represent in reality (see Branch & Wheeler 2017, and references therein). Another possibility is the violent merger scenario, arising from DD systems, where the merger of two sub-Chandra C/O WDs could lead to a super-Chandra explosion (e.g., Pakmor et al. 2012, 2013).

Motivated by the observational findings mentioned above, a considerable number of Ia explosion models that involve sub-Chandra $(0.9 \le M \le 1.2 M_{\odot})$, Blondin et al. 2017; Shen et al. 2018; Polin et al. 2019) WDs have been published recently (see, e.g., Liu et al. 2023, and references therein). Their common feature is the capability of modeling the ignition of the thermonuclear explosion self-consistently, without the need for an artificial triggering or a by-hand implementation of the deflagration-to-detonation transition, either via double-detonation (DuDe, i.e., triggering the explosion of the C/O WD by the detonation of a $\sim 0.01 M_{\odot}$ He layer on top of the WD), or by the "dynamically driven DD double-detonation" (D⁶, i.e., He-detonation caused by the merging of a C/O and a He-C/O WD) mechanism. Confronting the predictions of these models with the observations may advance our understanding about the true nature of these exotic explosions.

The goal of the present paper is the continuation of the work by Könyves-Tóth et al. (2020), hereafter referred as KTR20, by extending the photometric sample of SNe Ia with more well-observed objects, to derive constraints on the physical properties of SNe Ia, especially the ejecta mass, by combining photometric and spectroscopic data. In Section 2 we describe the new observational data used in this paper. In Section 3 we present the applied methods for distance determination, while Section 4 contains the details about the construction of the bolometric light curves. The method of inferring the physical parameters from the observations is described in Section 5. The

results are presented and discussed in Section 6, while in Section 7 we summarize our conclusions.

2. Data

In this section we present the observational data, the instruments utilized for the present study and the applied data reduction methods.

2.1. Observations

We carried out photometric observations of 28 Type Ia SNe between 2019 and 2023 from the Piszkéstető mountain station of Konkoly Observatory, Hungary in order to continue the photometric study of SNe Ia presented in KTR20. Our selection criteria for the sample SNe were the following:

- 1. decl. above -15° , in order to be observable from Piszkéstető station.
- 2. Low redshift, i.e., 0 < z < 0.1. The minimum redshift in the sample is z = 0.003, while the maximum is z = 0.07.
- 3. Pre-maximum discovery date in order to get reliable estimates on the rise time of the LCs.
- 4. Follow-up observations up to at least 40 days after maximum light.

From the overall sample of 28 objects, 21 exploded in spiral galaxies, 3 in lenticular galaxies, 3 in ellipticals and 1 host has unknown morphology.

The data were taken using the 0.8 m Ritchy–Chrétien (RC80) telescope of Konkoly Observatory, manufactured by the AstroSysteme Austria. RC80 is equipped with a 2048 \times 2048 back-illuminated FLI PL230 CCD chip that has 0."55 pixel scale and Johnson–Cousins *BV* and Sloan *griz* filters. This instrument is appropriate to obtain photometry for nearby (z < 0.1) Type Ia SNe with acceptable photometric signal-to-noise of \gtrsim 10.

There is an identical telescope, called BRC80, located at Baja Observatory of the University of Szeged, Hungary. Photometric data for two objects in the sample (SN 2021afsj and SN 2022fw) were obtained with this instrument. In the case of two other SNe (SN 2019bkh and SN 2019np) we also used some frames taken with the 0.6/0.9 m Schmidt telescope of the Piszkéstető Observatory using Johnson–Cousins *BVRI* filters, in order to extend the pre-maximum coverage of their LCs. The technical details of the Schmidt telescope can be found in KTR20, Section 2.

The basic data of the studied SNe Ia are collected in Table 1. The total (Milky Way plus host) reddenings ($E(B-V)_{\rm tot}$) and the luminosity distances (D_L) were derived by fitting the SN LCs with MLCS2k2 and SALT3 (see Section 3 for details). The color-combined gri images of the studied SNe are displayed in Figures 1 and 2.

2.2. Reduction and Photometry

The basic data reduction steps (bias, dark and flatfield corrections) were done in the standard way using the appropriate tasks in IRAF²⁰ (Image Reduction and Analysis Facility). The frames were then registered and median-combined to produce a single frame in each filter (see, e.g., Vinkó et al. 2018).

Except in a few cases, when the supernova occurred so far away from its host galaxy that it was unaffected by the host galaxy background, we applied image subtraction photometry to separate the light of the host galaxy from the light of the transient. Since we do not have images with the RC80 telescope taken before or sufficiently late after explosion, we used frames from the PanSTARRS-1 (PS1) imaging archive (Flewelling et al. 2020) for the image subtraction process. Before subtracting the PS1 images, we applied the IRAF geomap, gregister, psfmatch and linmatch tasks to crop, rotate, and scale the PS1 images to match the reduced RC80 frames. After removing the host from the frames, we determined the apparent magnitude of the SN and multiple local comparison stars in each filter via aperture photometry. We used the cataloged PS1 magnitudes of the comparison stars for transforming the instrumental magnitudes to the standard system in the standard way, including color terms in the transformation. For the B and V data the g_{PS1} and r_{PS1} magnitudes of the comparison stars were transformed into Johnson–Cousins B and V magnitudes based on the formulae given by Tonry et al. (2012).

Finally, the uncertainties of the obtained magnitudes were calculated as the squared sum of the photometric errors given by IRAF, and the fitting errors from the standard transformation.

All photometric data can be found online in the following GitHub repository: https://github.com/borazso/PiszkeSN.

2.3. Spectroscopy

In order to determine expansion velocities (see Section 5.1), we used spectra obtained with the instruments at Las Cumbres Observatory (LCO) and McDonald Observatory (Table 2).

The LCO spectra were taken with the FLOYDS spectrographs mounted on the LCO 2 m telescopes, via the Global Supernova Project (GSP). The spectra were reduced by a custom pipeline using IRAF tasks (Valenti et al. 2014). Additional data were taken with the Low Resolution Spectrograph 2 (LRS2) on the 10 m Hobby-Eberly Telescope (HET) at McDonald Observatory (Chonis et al. 2016). Since the Si II λ 6355 line, which was used for the velocity measurements, falls within the wavelength coverage of the blue arm (LRS2-B,

²⁰ IRAF is distributed by the National Optical Astronomy Observatories, which are operated by the Association of Universities for Research in Astronomy, Inc., under cooperative agreement with the National Science Foundation http://iraf.noirlab.edu.

3640–6970 Å), we used spectra taken with LRS2-B. The spectra were extracted from the IFU data cubes by the Panacea²¹ pipeline. The extracted spectra were then corrected for redshift and telluric lines using Python scripts and IRAF tasks.

2.4. Public Databases

We collected additional data to supplement our observations from two sources. We used public photometry from the Zwicky Transient Facility (ZTF) (Bellm et al. 2019) for 7 SNe SN 2019ein, (SN 2019bkh, SN 2020fob, SN 2020hvq, SN 2020tug, SN 2020uxz, SN 2021ytp), where the RC80 LCs did not cover the pre-maximum phases. Since our goal is to determine the physical parameters of these supernovae, wide phase coverage of the LCs is crucial. Additionally, some physical parameters of the explosion can only be determined by examining the late-time tail of the light-curve. Therefore in the case of 3 SNe (SN 2019ein, SN 2020tug, SN 2020uxz), we used the public ZTF photometry to extend their LCs into later phases. The downloaded ZTF data can be found in the GitHub repository²² of this paper. We also collected all available public spectra for our sample SNe from the Transient Name Server (TNS).²³ All spectroscopic data are shown in Table 2. Details on determining the expansion velocities from these spectra are given in Section 5.1.

3. Distance Estimates

In this section, we describe our methods to estimate the distances and reddenings of our sample SNe Ia by applying two different techniques and codes: SALT3 (see Section 3.1) and MLCS2k2 (Section 3.2).

3.1. SALT3

In the present paper we utilized the SALT3 code, which is the improved version of SALT2 (Spectral Adaptive Lightcurve Template; Guy et al. 2005, 2007, 2010; Betoule et al. 2014).

In SALT3 the spectral flux of the supernova is expressed as a function of wavelength (λ) and the rest-frame phase (p) as

$$F(p, \lambda) = x_0 \cdot [M_0(p, \lambda) + x_1 \cdot M_1(p, \lambda)] \cdot \exp(c \cdot CL(\lambda)),$$
(1)

where M_0 , M_1 , and CL are the calibrated template vectors, while the fitting parameters are the flux normalization x_0 , the stretch parameter x_1 and the color parameter c.

Here we adopt the most recent template vectors by Kenworthy et al. (2021), which were trained with \sim 1200 spectra covering the wavelength range of 2000 and 11000 Å. This sample is more than an order of magnitude larger

compared to the training sets of previous version of the code, thus, SALT3 has lower uncertainties than, e.g., SALT2.4 (Taylor et al. 2023). In 2022, the SALT3 code was extended further into the near-infrared by Pierel et al. (2022).

In the SALT3 framework the luminosity distances to SNe Ia can be derived in two main steps. First, the three free parameters $(x_0, x_1, \text{ and } c)$ are found from fitting Equation (1) to a particular SN Ia light curve. Second, their best-fit values are substituted into the Tripp-equation (Tripp 1998) to get the distance modulus μ :

$$\mu = m_B + \alpha x_1 - \beta c - M_B^0, \tag{2}$$

where m_B is the rest-frame B-band peak magnitude of the SN $(m_B = -2.5 \log_{10}(x_0) + m_0)$, α and β are the nuisance parameters representing the slopes of the stretch-luminosity and color-luminosity relations, while M_B^0 is the fiducial absolute magnitude of a SN Ia in the rest-frame B-band. Here we adopt $\alpha = 0.133 \pm 0.003$ and $\beta = 2.846 \pm 0.017$ from Pierel et al. (2022), and $M_B^0 = -19.253$ from Riess et al. (2022). We find $m_0 = 10.607$ by matching our best-fit m_B values to those of the Pantheon+SH0ES²⁴ SNe Ia sample (Riess et al. 2022). Note that we ignore second-order terms in Equation (2), like the mass-step $\delta \mu_{\text{host}}$ (Betoule et al. 2014; Brout et al. 2019), or the bias correction $\delta \mu_{\text{bias}}$ (Kessler et al. 2019), because for our low-z sample their values are smaller than the typical uncertainty of our distance modulus estimates (~ 0.1 mag).

The fitting was done with the SNcosmo²⁵ python library (Barbary et al. 2016), adopting Milky Way extinction estimates provided by the NASA/IPAC Infrared Science Archive (Schlegel et al. 1998; Schlafly & Finkbeiner 2011), and redshift information from the NASA Extragalactic Database (NED).²⁶ The best-fit values of t_0 , x_0 , x_1 and c for each supernova can be found in the GitHub repository of this paper (see above). The final luminosity distances (via μ from Equation (2)) are shown in Table 1.

3.2. MLCS2k2

Even though SALT3 provides accurate relative distances to SNe Ia via Equation (2), which are now tied to Cepheid-based absolute distances (Riess et al. 2022), the construction of the bolometric LCs require information about the extinction due to dust in the host galaxy of each SN. Since the SALT3 flux model (Equation (1)) incorporates the effect of dust extinction into the color parameter, it does not give a direct prediction of the dust extinction occurred in the host. Thus, we utilized the

²¹ https://github.com/grzeimann/Panacea

https://github.com/borazso/PiszkeSN

²³ https://www.wis-tns.org/

https://github.com/PantheonPlusSH0ES/DataRelease

²⁵ https://sncosmo.readthedocs.io/en/stable/

²⁶ The NASA/IPAC Extragalactic Database (NED) is funded by the National Aeronautics and Space Administration and operated by the California Institute of Technology.

Multi-Color Light Curve Shape Method (MLCS2k2; Riess et al. 1995, 1996; Jha et al. 2007) to overcome this difficulty.

Since MLCS2k2 was calibrated to Johnson–Cousins *UBVRI* photometry (Jha et al. 2007) we applied this code only to our Johnson B- and V-band data (after correcting them to Milky Way extinction, as above), and fixed both the distance modulus and the moment of the B-band maximum light from the results of our SALT3 fitting. This way we got reasonable estimates on the host galaxy extinction value A_V , from which we inferred the $E(B-V)_{host}$ reddening and the extinction in other passbands using the Milky Way reddening law parameter $R_V = 3.1$. Finally, the total reddening was calculated as $E(B-V)_{total} = E(B-V)_{MW} + E(B-V)_{host}$ (see Table 1). The best-fit MLCS2k2 parameters can be found in the GitHub repository²⁷ of this paper.

4. Bolometric Light Curves and their Modeling

In this section we briefly describe the construction of the bolometric LCs and the fitting of the radiation-diffusion Arnett models.

4.1. Bolometric Light Curve Construction

The bolometric LCs were constructed with the same methodology as in KTR20: briefly, after correcting the BVgri magnitudes (the z-band data were omitted due to their higher uncertainties) to the effect of dust extinction (both in the Milky Way and the host galaxy, see Table 1), the magnitudes were converted to flux densities, then corrected for distance and redshift. The resulting rest-frame absolute flux densities were then integrated along the wavelength axis by applying the trapezoidal rule. The missing UV- and IR-fluxes were approximated in a similar way as in KTR20, by assuming a linear decrease in flux from the wavelength of the B filter down to 1900 Å, and estimating the IR contribution by fitting a Rayleigh–Jeans tail to the i-band flux, then integrating it from the wavelength of the i-band filter to infinity. This method was extensively tested by KTR20 concluding that this technique gives a reliable representation of the true bolometric flux/ luminosity, and the relative uncertainty of the derived fluxes does not exceed $\sim 10\%$.

As mentioned above, in those cases when our observations did not cover the pre-maximum phases, we extended the LCs with public ZTF photometry. Since ZTF data are available only in g- and r-bands, applying the trapezoidal integration method leads to higher uncertainties in the resulting pseudo-bolometric fluxes. Thus, we tested the effect of omitting bands other than g and r from the integration using the high-cadence data of SN 2021hpr. We found that restricting the data only to g and r (but doing the correction for the missing bands as above) underestimates the integrated flux by only $\sim 2.8\%$ during the

pre-maximum phases compared to the case when the full BVgri data are integrated. The difference increases up to $\sim\!8\%$ around maximum light, then drops back to $\sim\!2.5\%$ later than +5 days from maximum. Since pre-maximum data are important to constrain the physical parameters of the light curve model, motivated by these experiments we decided to use the ZTF-based quasi-bolometric data in the final LCs, but assigned 50% larger error bars to those points in order to represent their higher uncertainty.

4.2. Model Fitting

The bolometric LCs were modeled applying the Monte-Carlo based Minim code (Chatzopoulos et al. 2013), which fits the radiation-diffusion model of Arnett (1982) to the quasi-bolometric LC of the SN. The following assumptions were adopted for the Arnett-model:

- 1. spherically symmetric, homologously expanding ejecta,
- 2. spatially constant density profile,
- 3. constant optical opacity, both spatially and temporally,
- 4. centrally located radioactive heating source,
- 5. radiation pressure being dominant,
- 6. the spatial temperature profile being fixed to the "radiative-zero" solution,
- 7. separation of the spatial and temporal part of the energy equation.

The Minim code uses the Price-algorithm in order to localize the absolute minimum of the χ^2 surface in the parameter space within pre-selected parameter bounds. The detailed description of the code and its method to estimate the uncertainties of each fitted parameter values can be found in Chatzopoulos et al. (2013).

The SNe Ia LCs were fitted with the usual model of radioactive decay of $^{56}\text{Ni} \rightarrow ^{56}\text{Co} \rightarrow ^{56}\text{Fe}$ by optimizing the following four parameters (e.g., KTR20):

- 1. t_0 : the moment of the explosion with respect to the date of maximum brightness in the B-band (in days),
- 2. *t*_{LC}: the LC timescale, similar to the rise time to maximum (in days),
- 3. t_{γ} : the timescale of the gamma-ray leaking (in days),
- 4. $M_{\rm Ni}$: the initial nickel-mass (in M_{\odot}).

The best-fit model parameters are given in the first 4 columns of Table 3.

5. Physical Parameters

To determine the physical parameters for each SN, such as the ejecta mass $(M_{\rm ej})$ or the opacity (κ) , we used an improved version of the method presented in Li et al. (2019) and KTR20 (see Equations (3) and (4)). In the present paper the expansion velocity $v_{\rm exp}$ was estimated directly from spectra taken near maximum light (described in Section 5.1). By using the

²⁷ https://github.com/borazso/PiszkeSN

timescales t_{γ} and $t_{\rm LC}$ provided by the Minim code, we calculate the ejecta mass as

$$M_{\rm ej} = \frac{4\pi t_{\gamma}^2 \cdot v_{\rm exp}^2}{3\kappa_{\gamma}},\tag{3}$$

and the average opacity in the ejecta as

$$\kappa = \frac{t_{\text{LC}}^2 \cdot \beta c \cdot v_{\text{exp}}}{2M_{\text{ej}}},\tag{4}$$

where $\kappa_{\gamma} = 0.025 \ {\rm cm^2 \ g^{-1}}$ is the opacity for gamma-ray photons (Guttman et al. 2024), $\beta = 13.8$ is an integration constant related to the density distribution of the ejecta (Arnett 1982), and $v_{\rm exp}$ is the expansion velocity of the SN.

Furthermore, the kinetic energy of the expanding ejecta (assuming homologous expansion of a constant density sphere) can be expressed as

$$E_{\rm kin} = \frac{3}{10} M_{\rm ej} \cdot v_{\rm exp}^2. \tag{5}$$

5.1. Expansion Velocities

The expansion velocity, $v_{\rm exp}$, appearing in Equations (3)–(5), was estimated from optical spectra taken near maximum light (see Section 2.3): we used the Doppler-shift of the absorption minimum of the Si II λ 6355 feature in each available spectrum to measure the expansion velocity at the given phase. After correcting the spectra for the redshift of the host galaxy, the observed wavelength of the Si II feature was measured by fitting the absorption component with a single Gaussian function near the core, then taking the center of the fitted profile as the observed wavelength ($\lambda_{\rm obs}$). The Doppler-shift of $\lambda_{\rm obs}$ from the rest-frame position, $\lambda_0 = 6355$ Å, gives the Si II velocity ($\nu_{\rm Si~II}$). In this paper we adopted $\nu_{\rm Si~II}$ measured at maximum light as an estimate for $\nu_{\rm exp}$.

For those SNe that had available spectra taken close to maximum, the determination of $v_{\rm exp}$ was relatively easy. However, this was not the case for most of our sample SNe. In these cases we had to interpolate between the $v_{\rm Si~II}$ values measured at different phases in order to get the velocity near maximum light. The interpolation was done using a pre-defined set of exponential functions fitted to the measured $v_{\rm Si~II}$ velocities of the well-observed SN 2019ein (a high-velocity SN Ia) and SN 2011fe (a normal velocity SN Ia).

For SN 2019ein we used the spectra listed in Table 2, while for SN 2011fe we collected the spectra from Pereira et al. (2013). First, the measured velocities of these two SNe as a function of time were fitted with exponential functions. Then, 100 other exponentials were computed to model the temporal evolution of the velocity within the range defined by SN 2011fe and SN 2019ein (plotted with gray dotted curves in Figure 3). The parameters of these exponentials were computed starting

from 90% of the parameters of SN 2011fe, extending up to 110% of the parameters of SN 2019ein.

To estimate the velocity at the moment of maximum light for a given SN, first, we plotted the measured velocities against phase, then looked for the best-fitting pre-defined exponential that was closest to the measured velocities. Then, using the parameters of this exponential we inferred its value at zero phase, i.e., at the moment of maximum light in the *B*-band (see the blue dashed curve in Figure 3 as an example for SN 2021hpr).

This method worked well in those cases when only 1 or 2 spectra were available. However, for SNe with multiple spectra available, we found that some of them showed a velocity evolution that was slightly different from the pre-defined exponential functions. Thus, in those cases we preferred fitting the measured velocities with another exponential function and using this best-fit exponential to estimate the velocity at maximum light. This fitting introduces a small ($\sim 200 \, \mathrm{km \, s^{-1}}$) error and so the uncertainty of the Si II velocity at maximum light comes in most part from the uncertainty of how well we can find the line minima in the individual spectra.

Figure 4 summarizes the measured velocities (colored symbols) as well as their best-fitting exponential functions (dotted curves). The two solid curves represent SN 2011fe and SN 2019ein.

5.2. Classification of the Sample SNe Into Subtypes

One of the most important parameters of a SN Ia is its color, which is especially interesting in the early phases: it can be a good tracer of the presence of interaction with a companion star (Kasen 2010), double detonation explosion (Polin et al. 2019), or ⁵⁶Ni-mixing near the surface (Magee & Maguire 2020).

After correcting for Milky Way and host galaxy extinction, we constructed the $(B-V)_0$ color curves of our sample, and estimated the color at the moment of maximum light by fitting a quadratic function to their color evolution.

Many studies have been proposed to further divide SNe Ia into several subclasses based on their spectroscopic and photometric properties; see, e.g., Benetti et al. (2005), Branch et al. (2006, 2009), Wang et al. (2009), Stritzinger et al. (2018). The Stritzinger et al. (2018) classification separates SNe Ia based on their early (≤4-5 days after explosion) color evolution: SNe showing $(B - V)_0 \ge 0.2$ mag at around +2 days belong to the early red group, while objects showing $(B-V)_0 < 0.05$ mag are considered as the members of the early blue group. According to Benetti et al. (2005), early red SNe Ia are often associated with Branch Core Normal (CN) and Cool (CL) types showing low velocity gradient (LVG), while early blue objects are usually classified as LVG Shallow Silicon (SS), also known as SNIa-91T subtype. The Wang et al. (2009) scheme separates SNe Ia based on their $v_{Si,II}$ velocity at maximum light: High Velocity (HV) SNe have $v_{\mathrm{Si\ II}} \gtrsim 12,000\ \mathrm{km\ s^{-1}}$, while Normal Velocity (NV) SNe show $v_{\mathrm{Si\ II}} \approx 10,600\ \mathrm{km\ s^{-1}}$ (see also Branch & Wheeler 2017, for further details and references). The Si II velocity has also been found by Wang et al. (2013) to be connected to the environment of SNe Ia, with HV events originating from younger, more metal-rich surroundings than NV events.

By using the estimated v_{exp} at maximum and the early $(B-V)_0$ color curves, we determined the Wang et al. (2009) and Stritzinger et al. (2018) subtypes for the sample SNe where it was possible. Unfortunately, only 7 objects (SNe 2019ein, 2020rqk, 2020tug, 2020uxz, 2021hpr, 2021rhu, 2022fw) had photometry taken at sufficiently early phases to determine their Stritzinger et al. (2018) group. 5 SNe out of 7 (SNe 2019ein, 2020uxz, 2021hpr, 2021rhu and 2022fw) were found to be consistent with the criteria for the early red subgroup, and the remaining 2 (SNe 2020rqk and 2020tug) belong to the early blue subgroup. Applying the Wang et al. (2009) classification, most SNe in our sample were found to be of normal velocity (NV) type, and only 6 of them (SNe 2019cth, 2019ein, 2020hvq, 2021wuf, 2021ytp and 2022hrs) belonged to the high velocity (HV) group. It was, however, recently argued that SN 2021hpr may be a transitional object between the Wang NV and HV objects being at the lower end of the HV regime (Zhang et al. 2022).

5.3. Ejecta Masses

Finally, from Equations (3)–(5) we inferred the ejecta masses, ejecta opacities and kinetic energies of each SNe Ia in our sample. The results are summarized in Table 3.

6. Discussion

In this section we present constraints and correlations between the physical parameters and progenitor systems of the studied SNe Ia, and discuss their implications for the explosion mechanisms.

6.1. Comments on Individual Objects

In this subsection we discuss and compare our results with those obtained by others for some individual SNe in our sample. The objects listed here are the ones that either had published results that were comparable to our work, or they were found to have some peculiarities during our analysis.

1. SN 2019ein: We classified SN 2019ein as a high velocity SN Ia, consistent with Kawabata et al. (2020) and Xi et al. (2022). Additionally, Xi et al. (2022) estimated a nickel mass of $0.27-0.31\,M_\odot$, which is lower than our result of $0.44\pm0.05\,M_\odot$. The reason for the disagreement is most likely the $\sim\!0.4\,\mathrm{mag}$ lower distance modulus adopted in the previous papers. Xi et al. (2022) also proposed that SN 2019ein might be the result of a sub-Chandra double detonation explosion. Pellegrino et al.

- (2020) also estimated a nickel mass of $0.33\,M_{\odot}$, which, again, is lower than our result, but it was based on spectral modeling instead of photometry. Contrary to Xi et al. (2022), they argue that this event is a product of the delayed-detonation scenario. Our estimated ejecta mass for SN 2019ein is $1.12\pm0.18\,M_{\odot}$, which is consistent with a sub-Chandra explosion, but because of the relatively high uncertainty of the ejecta mass, the possibility for a Chandrasekhar-mass delayed-detonation explosion cannot be excluded.
- 2. SN 2019cth: SN 2019cth was a 91T-like event, but with low maximum luminosity and low nickel mass, contrary to the expectations. The reason for the inconsistency could be due to the poor phase coverage of our data around maximum light. The uncertainty of the nickel mass is also significant: the value given by the Minim fitting $(0.64 \pm 0.08~M_{\odot})$ is significantly higher than the one calculated by the method of Khatami & Kasen (2019) $(0.46 \pm 0.01~M_{\odot})$. Thus, the parameters for this object listed in Table 3 should be considered with caution.
- 3. SN 2019np: Sai et al. (2022) also applied the Minim code and the Arnett-model to fit the quasi-bolometric light curve of SN 2019np, which resulted in a nickel mass of $0.66 \pm 0.05 \, M_{\odot}$. This value is slightly lower than our $M_{\rm Ni} = 0.75 \pm 0.05 \, M_{\odot}$. From spectroscopy Sai et al. (2022) estimated the ejecta velocity as \sim 10,200 km s⁻¹ at B-band maximum, which agrees with our value within the errors. On the other hand, they estimated a high ejecta mass of $\sim 1.34 \pm 0.12 \, M_{\odot}$ compared to our value of $\sim 1.01 \pm 0.08 \, M_{\odot}$. However, inserting their reported $v_{\rm exp}$ and t_{γ} values into Equation (3), we get an ejecta mass of $\sim 0.9 \, M_{\odot}$. Thus, we believe that the ejecta mass reported by Sai et al. (2022) is an overestimate, if we use their parameters at face value. They also found extra light in the early phases of the light curve, and attribute it to nickel-mixing. Our data were not taken early enough to confirm their finding.
- 4. SN 2020hvq: This SN appeared right in the dust lane of the edge-on galaxy UGC 10561 (see Figure 1). Our data on SN 2020hvg extend well beyond +80 days, but the Minim code could not fit the tail beyond +60 days well. This may have resulted in an overestimate of the t_{γ} value. The best-fit $t_{\gamma} \sim 50$ days is not extremely long, but coupled with the relatively high expansion velocity, $v_{\rm exp} \approx 13,900 \, {\rm km \, s^{-1}}$, gives a very high ejecta mass of $M_{\rm ei} \approx 3 \, M_{\odot}$. Such a high ejecta mass is inconsistent with not only the current explosion models for SNe Ia, but also with the t_{LC} parameter (\sim 10.6 days) that would imply $M_{\rm ej} \approx 1.2 \, M_{\odot}$ according to the method by KTR20. The long t_{γ} could be due to some extra light in the late-phase photometry, either by the insufficient subtraction of host galaxy background from our frames, a light echo on significant dust content in the host around the line of

Table 1Basic Data of the Studied SNe Ia

SN	R.A.	Decl.	E(B-V)	E(B-V)	Discovery	Host Galaxy	z	Туре	$D_{ m L}$
	(hh:mm:ss)	(dd:mm:ss)	(MW, mag)	(total, mag)					(Mpc)
SN 2019bkh	13:08:57.4	+28:16:52.4	0.009	0.119	2019-03-03	MCG +05-31-141	0.0195	Ia-norm	113.2 (2.2)
SN 2019ein	13:53:29.1	+40:16:31.3	0.010	0.020	2019-05-01	NGC 5353	0.0078	Ia-norm	42.2 (0.8)
SN 2019cth	14:45:47.5	+50:23:48.3	0.024	0.063	2019-04-03	IC 1056	0.0134	Ia-91T	63.4 (1.3)
SN 2019np	10:29:22.0	+29:30:38.3	0.017	0.088	2019-01-09	NGC 3254	0.0044	Ia-norm	32.6 (0.6)
SN 2020enm	16:35:06.8	+46:12:53.3	0.015	0.137	2020-03-16	IC 1222	0.0308	Ia-91T	141.3 (2.7)
SN 2020fob	07:43:08.8	+45:21:49.4	0.042	0.055	2020-03-30	CGCG 235-032	0.0315	Ia-norm	150.7 (3.5)
SN 2020hvq	16:46:34.9	+62:49:36.8	0.036	0.077	2020-04-21	UGC 10561	0.0190	Ia-norm	97.0 (3.6)
SN 2020rqk	16:00:58.5	+70:36:15.0	0.026	0.058	2020-08-19	NGC 6071	0.0239	Ia-norm	117.4 (2.2)
SN 2020tug	23:59:27.9	+17:51:54.7	0.025	0.080	2020-09-19	KUG 2356+175	0.0500	Ia-norm	247.5 (7.6)
SN 2020ue	12:42:46.8	+02:39:34.1	0.024	0.024	2020-01-12	NGC 4636	0.0030	Ia-norm	16.4 (0.3)
SN 2020uxz	01:24:06.9	+12:55:17.2	0.033	0.033	2020-10-05	NGC 514	0.0083	Ia-norm	38.7 (0.7)
SN 2021accx	23:40:01.6	+27:16:37.4	0.083	0.112	2021-10-23	J234001.30+271626.4 ^a	0.0310	Ia-norm	144.8 (2.5)
SN 2021afsj	08:56:42.4	+52:06:28.8	0.017	0.124	2021-11-29	UGC 4671	0.0122	Ia-norm	60.8 (1.4)
SN 2021dov	08:56:18.7	-00:26:31.7	0.030	0.282	2021-02-22	Z 5-38	0.0127	Ia-91T	58.7 (1.0)
SN 2021gtp	08:48:50.3	+29:52:13.8	0.035	0.235	2021-03-19	UGC 04611	0.0197	Ia-norm	94.2 (3.5)
SN 2021hiz	12:25:41.7	+07:13:42.2	0.022	0.116	2021-03-30	UGC 7513	0.0033	Ia-norm	27.9 (0.5)
SN 2021hpr	10:16:38.6	+73:24:01.8	0.022	0.109	2021-04-02	NGC 3147	0.0094	Ia-norm	46.8 (1.2)
SN 2021rhu	00:03:15.4	+16:08:44.5	0.038	0.129	2021-07-01	NGC 7814	0.0035	Ia-norm	16.6 (0.3)
SN 2021ucm	23:35:30.4	+12:25:27.9	0.059	0.166	2021-07-25	J233530.78+122531.4a	0.0240	Ia-norm	113.7 (2.3)
SN 2021wuf	17:56:02.5	+18:21:14.1	0.078	0.091	2021-08-23	NGC 6500	0.0100	Ia-91T	44.2 (1.0)
SN 2021yrf	03:38:40.2	+38:01:17.7	0.329	0.387	2021-09-09	CGCG 525-046	0.0166	Ia-norm	86.1 (1.6)
SN 2021ytp	17:33:11.0	+22:26:27.1	0.049	0.153	2021-09-09	J173310.37+222637.5 ^a	0.0650	Ia-norm	279.7 (4.5)
SN 2022aaiq	14:26:32.0	+56:35:03.1	0.017	0.146	2022-11-15	NGC 5631	0.0065	Ia-norm	35.8 (1.9)
SN 2022fw	12:23:54.0	-03:26:37.9	0.032	0.290	2022-01-09	NGC 4348	0.0067	Ia-norm	31.4 (1.2)
SN 2022 hrs	12:43:34.3	+11:34:35.8	0.023	0.188	2022-04-16	NGC 4647	0.0047	Ia-norm	19.1 (0.3)
SN 2022ydr	17:38:56.8	+74:49:48.5	0.032	0.032	2022-10-18	UGC 10949	0.0249	Ia-91bg	133.8 (5.5)
SN 2022zut	11:40:58.8	+11:28:10.9	0.038	0.325	2022-11-09	NGC 3810	0.0033	Ia-norm	18.8 (0.4)
SN 2023bee	08:56:11.6	-03:19:32.0	0.014	0.014	2023-02-01	NGC 2708	0.0067	Ia-norm	37.5 (1.1)

Note.

sight, or a late-time circumstellar interaction (Terwel et al. 2024). Because SN 2020hvq is a significant outlier in our sample, it was excluded from further analysis.

- 5. SN 2020tug: Similar to SN 2019cth, this object lacked near-maximum observations in our data, thus, the estimated nickel mass may be more uncertain.
- 6. SN 2021dov: SN 2021dov is a 91T-like SN Ia, which showed the highest maximum luminosity in our sample $(\sim 2 \times 10^{43} \, \mathrm{erg \, s^{-1}})$. As expected, this implies a high nickel mass of $\sim 1.2 \, M_{\odot}$. However, the inferred ejecta mass was found to be unexpectedly low, $0.93 \pm 0.15 \, M_{\odot}$. Since the condition $M_{\mathrm{Ni}} > M_{\mathrm{ej}}$ is unphysical, we suspect that in this case some of the initial assumptions, probably the centrally located powering source, of the Arnettmodel fails (see Section 6.5 for further discussion). Significant interaction with a H-poor CSM that increases the maximum luminosity beyond the radioactive heating, or a non-spherically expanding ejecta are also possible explanations. Note that KTR20 also found a similar
- outlier (SN 2017erp) in their sample, which showed $M_{\rm Ni} \approx M_{\rm ej}$.
- 7. SN 2021hpr: Lim et al. (2023) observed excess light in the early LC, and attributed this to the shock-heated cooling emission (SHCE) that arises from interaction with a companion star. Using the SHCE model along with delayed-detonation models, they were able to fit the early LC adequately. While the double-detonation model of Polin et al. (2019) also predicts extra light in the early LC, Lim et al. (2023) found that it does not fit the observations as well as the SHCE model. SN 2021hpr is the third SN Ia discovered in NGC 3147 during the last half-century. A study of SN 2021hpr and its siblings were presented by Barna et al. (2023), who also used the data from the RC80 and BRC80 telescopes, but performed their own independent analysis. Their estimated nickel mass $(0.44 \pm 0.14 \, M_{\odot})$ is lower than the value given in Table 3 (0.67 \pm 0.05 M_{\odot}), but their expansion velocity $(11,200 \pm 1200 \,\mathrm{km \, s^{-1}})$, and ejecta mass $(1.12 \pm 0.28 M_{\odot})$ are both in agreement with

^a Host galaxy names in the SDSS catalog.

Table 2
Spectroscopic Data for the Sample SNe

SN	Date (XXXX MM DD)	Phase	V _{exp.}	Source
	(YYYY-MM-DD)	(days)	(km s^{-1})	
SN 2019bkh	2019-03-04	-10.75	13753 (17)	TNS: ZTF (Fremling et al. 2019a)
ar an a	2019-03-05	-9.77	13362 (749)	TNS: Padova-Asiago (Fiore et al. 2019)
SN 2019cth	2019-04-24	0.32	13577 (81)	LCO GSP
SN 2019ein	2019-05-02	-14.65	22794 (959)	TNS: Global SN Project (Burke et al. 2019b)
	2019-05-05	-11.68	19075 (817)	TNS: ZTF (Fremling et al. 2019b)
	2019-05-12	-4.73	14436 (559)	TNS: Pascal Le Dû (Du 2020)
	2019-05-14	-2.75	13759 (285)	TNS: Pascal Le Dû (Du 2020)
	2019-05-16	-0.76	12874 (433)	LCO GSP
CN 2010	2019-05-21	+4.20	12156 (446)	TNS: Pascal Le Dû (Du 2020)
SN 2019np	2019-01-10	-17.35	14672 (156)	TNS: Global SN Project (Burke et al. 2019a)
	2019-01-10	-16.66 -15.36	14973 (400)	TNS: YNAO (Wu et al. 2019)
	2019-01-12	-13.36 -3.41	13623 (759)	TNS: ZTF (Dahiwale & Fremling 2020a)
CN 2020amm	2019-01-24		10030 (85)	LCO GSP
SN 2020enm	2020-03-18	-11.83	11438 (937)	TNS: YNAO (Zhang & Wang 2020)
SN 2020fob	2020-03-31	-7.76	11545 (933)	TNS: ZTF (Dahiwale & Fremling 2020b)
SN 2020hvq	2020-04-22	-11.42	17033 (587)	TNS: ISSP (Balcon 2020)
CNI 20201-	2020-04-23	-10.40	17129 (1303)	TNS: ZTF (Dahiwale & Fremling 2020c)
SN 2020rqk	2020-08-16	-15.66	13975 (887)	TNS: ZTF (Yang et al. 2020)
SN 2020tug	2020-09-22	-13.38	15007 (589)	TNS: adH0cc (Floers et al. 2020)
GN 2020	2020-10-05	-1.00	9612 (1139)	LCO GSP
SN 2020ue	2020-01-28	2.20	10875 (588)	LCO GSP
SN 2020uxz	2020-10-05	-17.22	15160 (282)	TNS: Global SN Project (Burke et al. 2020)
CNI 2021	2020-10-20	-2.35	10493 (97)	LCO GSP
SN 2021accx	2021-10-28	-8.16	10816 (748)	TNS: ePESSTO+ (Ihanec et al. 2021)
	2021-11-06	0.57	9887 (283)	LCO GSP
CNI 2021 of ai	2021-11-11	+5.42	9907 (283)	HET
SN 2021 des	2021-11-30	-13.18	12681 (1502)	TNS: ISSP (Balcon 2021)
SN 2021dov	2021-03-12	+0.19	10478 (388)	LCO GSP
CNI 2021 -4	2021-03-21	+9.08	8916 (184)	TNS: PSH (Grzegorzek 2021a)
SN 2021gtp SN 2021hiz	2021-03-22	-13.75 -16.62	16957 (1654)	TNS: ZTF (Dahiwale & Fremling 2021)
SIN 2021IIIZ	2021-03-31	-16.62 +0.32	14607 (736)	TNS: SUCSC (Dimitriadis et al. 2021) LCO GSP
SN 2021har	2021-04-17		9787 (309)	TNS: Three Hills Observatory (Leadbeater 2021)
SN 2021hpr	2021-04-03	-15.88 -14.89	19246 (678)	TNS: Three Hins Observatory (Leadbeater 2021) TNS: ZTF (Perley 2021)
	2021-04-04	-0.03	18933 (972)	· · · · · · · · · · · · · · · · · · ·
SN 2021rhu	2021-04-19 2021-07-01	-0.03 -14.94	11136 (29)	TNS: PSH (Grzegorzek 2021b) TNS: ALeRCE (Atapin et al. 2021)
31 2021111u	2021-07-01	-14.94 -10.96	17158 (126)	TNS: ZTF (SNIascore 2021)
	2021-07-03	-10.90 -1.99	13036 (1038) 11600 (263)	LCO GSP
	2021-07-14	+5.98	10479 (489)	HET
	2021-07-28	+11.96	9806 (1577)	HET
SN 2021ucm	2021-07-28	-6.88	13374 (161)	TNS: ePESSTO+ (Pessi et al. 2021)
51V 2021 UCIII	2021-08-02	-6.34	13091 (1277)	TNS: SCAT (Jaeger 2021)
SN 2021wuf	2021-08-02	-10.65	19400 (4546)	TNS: SCAT (Huber 2021)
511 2021 wui	2021-09-06	+1.23	12270 (511)	LCO GSP
SN 2021yrf	2021-09-13	-11.65	16274 (1771)	TNS: ATLAS (Srivastav et al. 2021)
SN 2021ytp	2021-09-15	-6.10	16489 (328)	TNS: ePESSTO+ (Deckers et al. 2021)
SN 2022aaiq	2022-11-17	-12.26	11253 (349)	TNS: LICK-UCSC (Siebert et al. 2022)
51 (2022aaaq	2022-12-12	+12.58	9391 (503)	TNS: ISSP (Balcon 2022c)
SN 2022fw	2022-01-10	-14.76	13240 (126)	TNS: Global SN Project (Hosseinzadeh et al. 2022
	2022-01-10	-13.76	12853 (583)	TNS: ePESSTO (Ramirez et al. 2022)
SN 2022 hrs	2022-01-11	-15.70 -15.07	16821 (2122)	TNS: ISSP (Balcon 2022a)
J., 2022 1110	2022-04-10	-10.10	14353 (705)	TNS: PSH (Grzegorzek 2022)
	2022-04-21	-2.13	12587 (943)	LCO GSP
SN 2022ydr	2022-04-29	-2.13 -5.94	10159 (510)	TNS: NOT/ALFOSC (V et al. 2022)
511 2022ydi	2022-10-23	-3.94 -3.99	10688 (788)	TNS: ISSP (Balcon 2022b)
	2022-10-27			
SN 2022zut	2022-11-10	-12.31	17423 (797)	TNS: SGLF/LTbot (Perez-Fournon et al. 2022)

Table 2 (Continued)

SN	Date (YYYY-MM-DD)	Phase (days)	(km s^{-1})	Source
	2022-11-17	-5.33	12997 (45)	HET
	2022-11-23	+0.65	10827 (194)	LCO GSP
SN 2023bee	2023-02-01	-17.80	23658 (1763)	TNS: LiONS (Zhai et al. 2023)
	2023-02-02	-16.81	22207 (1941)	TNS: Global SN Project (Hosseinzadeh et al. 2023)
	2023-02-11	-7.87	12150 (40)	HET
	2023-02-16	-2.90	11461 (45)	LCO GSP
	2023-02-17	-1.91	11444 (358)	HET

our values (see Table 3). The disagreement in the nickel mass can be traced back to their lower adopted extinction and distance modulus.

- 8. SN 2021rhu: SN 2021rhu was a sub-luminous and very red event near maximum compared to the other SNe in our sample. According to Harvey et al. (2023), it may represent a transitional object between normal and 91bglike SNe Ia, i.e., a 86G-like object. By modeling its spectra, Harvey et al. (2023) found that a delayeddetonation scenario is more likely than a doubledetonation explosion. In this paper, we estimate a nickel mass of $\sim 0.45 \, M_{\odot}$, which is close to the calculated $\sim 0.74\,M_{\odot}$ ejecta mass. The low ejecta mass is a consequence of the low t_{γ} value (~31 days), which is one of the lowest in our sample. Since the low t_{γ} and $M_{\rm ei}$ values seem to be relatively well-constrained and consistent with SN 2021rhu being a lower mass object, we speculate that the too low ejecta mass might be due to the failure of the Arnett-model, e.g., because of the unusual Ni-distribution (see Section 6.5).
- 9. SN 2022hrs: A SALT3 fitting of the *BVri* LC of SN 2022 hrs taken by 0.4 m LCO telescopes was recently published by Risin et al. (2023). They got significantly lower Ni-mass ($\sim 0.16\,M_\odot$) compared to our result ($\sim 0.6\,M_\odot$, Table 3). The disagreement is probably due to their different methodology: they used the best-fit LC amplitude provided by SALT3 to estimate the Ni-mass, while our result was inferred from the quasi-bolometric luminosities. Nevertheless, their result seems to be an underestimate compared the usual range of nickel masses in SNe Ia $(0.3-1.1\,M_\odot)$.
- 10. SN 2022ydr: Our observations of SN 2022ydr lack adequate coverage in the pre-maximum period, and the observations only extend until \sim 30 days after maximum. This can cause an uncertain fitting of the t_{γ} parameter, which in turn may lead to the low ejecta mass estimate of \sim 0.49 \pm 0.12 M_{\odot} , making it the only object in our sample that lies significantly below the sub-Chandra explosion models. SN 2022ydr was of a Ia-91bg subtype, and accordingly it had the lowest maximum luminosity

 $(\sim 0.55 \times 10^{43} \, {\rm erg \, s^{-1}})$, which is reflected in the relatively low $(\sim 0.24 \, M_{\odot})$ nickel mass with respect to the rest of the sample. Compared to most 91bg-like SNe, the Nimass of SN 2022ydr is a bit higher, but not unprecedented. For example, Sullivan et al. (2011) used Arnett's rule to estimate $\sim 0.2 \, M_{\odot}$ of ⁵⁶Ni for SN 2007au that had a peak luminosity similar to that of SN 2022ydr. It is possible that these higher-mass 91bg-like SNe Ia belong to a transitional group between 91bg and normal SNe Ia (Li et al. 2022). Another possibility is that at such low nickel masses the Arnett model might overestimate $M_{\rm Ni}$.

11. SN 2023bee: SN 2023bee was found to have excess blue light in the early part of the light-curve (Hosseinzadeh et al. 2023), which is most probably due to companion interaction (Kasen 2010).

6.2. Comparison with Other Works

In this subsection, we compare our methods and results to those given by previous publications.

6.2.1. Comparison with Khatami & Kasen (2019)

Instead of fitting the entire bolometric LC, Khatami & Kasen (2019) used only the maximum bolometric luminosity and the LC rise time to constrain the nickel mass. By using their method, we re-calculated the ⁵⁶Ni masses for the objects in our sample. Comparison of the nickel masses derived with the two different methods can be seen in Figure 5, which shows that the two methods give similar results, consistently with Bora et al. (2022). The consistency between the results from two different approaches that constrain the initial Ni-mass suggests that systematic errors of the estimated Ni-masses are not severe. It may strengthen the validity and applicability of the Arnett-model for most of the SNe Ia in the present sample.

6.2.2. Comparison with KTR20

As mentioned in Section 5, in the present paper we estimated the physical parameters of the studied SNe Ia similar to KTR20, except that the expansion velocities were inferred

Bora et al.

 Table 3

 Best-fit Physical Parameters of the Sample SNe

SN	t_{0}	$M_{ m Ni}$	$t_{ m LC}$	t_{γ}	$v_{\rm exp}$	$M_{ m ej}$	κ	$E_{ m kin.}$	$M_{ m Ni}^{ m KK19}$	Expl.
	(days)	(M_{\odot})	(days)	(days)	$(km s^{-1})$	(M_{\odot})	$(cm^2 g^{-1})$	(10^{51} erg)	(M_{\odot})	Model
SN 2019bkh	-16.4 (1.4)	0.70 (0.05)	12.40 (1.14)	43.80 (3.75)	10573 (383)	1.34 (0.33)	0.09 (0.04)	0.90 (0.22)	0.66 (0.01)	Both
SN 2019cth	-19.4(0.3)	0.64 (0.08)	19.57 (1.21)	36.64 (1.27)	13644 (81)	1.56 (0.13)	0.26 (0.05)	1.75 (0.14)	0.46 (0.01)	Near- $M_{\rm Ch}$
SN 2019ein	-15.6(0.4)	0.44 (0.05)	13.41 (0.32)	32.72 (1.14)	12927 (583)	1.12 (0.18)	0.16 (0.04)	1.12 (0.18)	0.41 (0.01)	Both
SN 2019np	-17.9(0.4)	0.75 (0.05)	16.21 (1.11)	41.28 (0.23)	9760 (350)	1.01 (0.08)	0.20 (0.05)	0.58 (0.05)	0.62 (0.01)	Sub- M_{Ch}
SN 2020enm	-13.2(2.2)	0.65 (0.06)	10.93 (1.23)	40.79 (0.82)	9449 (937)	0.93 (0.22)	0.09 (0.05)	0.50 (0.12)	0.59 (0.02)	Sub- M_{Ch}
SN 2020fob	-12.1(1.9)	0.26 (0.05)	8.26 (1.33)	37.20 (3.92)	10164 (933)	0.89 (0.35)	0.06 (0.05)	0.55 (0.22)	0.27 (0.01)	Both
SN 2020hvq	-15.3(0.5)	0.40 (0.05)	10.62 (0.83)	50.00 (2.33)	13881 (945)	3.01 (0.69)	0.04 (0.02)	3.48 (0.80)	0.42 (0.01)	Neither
SN 2020rqk	-15.9(0.1)	0.59 (0.05)	12.95 (0.40)	36.61 (1.17)	9602 (887)	0.77 (0.19)	0.16 (0.06)	0.43 (0.11)	0.57 (0.02)	Sub- M_{Ch}
SN 2020tug	-15.8(1.0)	0.70 (0.05)	11.06 (2.41)	41.69 (1.75)	9485 (864)	0.98 (0.26)	0.09 (0.07)	0.53 (0.14)	0.83 (0.01)	Both
SN 2020ue	-12.6(0.4)	0.34 (0.05)	9.57 (0.71)	34.45 (0.75)	11135 (588)	0.92 (0.14)	0.09 (0.03)	0.68 (0.10)	0.35 (0.01)	Sub- M_{Ch}
SN 2020uxz	-17.7(0.1)	0.63 (0.05)	14.39 (1.00)	43.60 (2.90)	10315 (190)	1.26 (0.22)	0.13 (0.04)	0.81 (0.14)	0.59 (0.01)	Both
SN 2021accx	-14.9(1.0)	0.66(0.05)	11.62 (1.43)	40.68 (1.97)	10008 (438)	1.04 (0.19)	0.10 (0.05)	0.62 (0.12)	0.61 (0.01)	Both
SN 2021afsj	-15.6(0.5)	0.64 (0.05)	12.79 (0.95)	38.28 (1.13)	9653 (1502)	0.85 (0.32)	0.14 (0.10)	0.48 (0.18)	0.59 (0.01)	Sub- M_{Ch}
SN 2021dov	-17.0(0.6)	1.19 (0.09)	14.59 (1.35)	39.42 (2.03)	9779 (286)	0.93 (0.15)	0.17 (0.06)	0.53 (0.09)	1.08 (0.01)	Sub- M_{Ch}
SN 2021gtp	-15.4(0.7)	0.69 (0.06)	12.80 (1.34)	37.64 (1.54)	10880 (1654)	1.05 (0.40)	0.13 (0.10)	0.74 (0.29)	0.66 (0.02)	Both
SN 2021hiz	-16.7(0.2)	0.59 (0.05)	14.98 (0.46)	37.38 (1.01)	9804 (523)	0.84 (0.14)	0.20 (0.06)	0.48 (0.08)	0.51 (0.01)	Sub- M_{Ch}
SN 2021hpr	-17.0(0.1)	0.67 (0.05)	13.97 (0.27)	39.96 (0.68)	11132 (560)	1.24 (0.17)	0.14 (0.03)	0.92 (0.12)	0.62 (0.01)	Both
SN 2021rhu	-14.5(0.1)	0.45 (0.05)	13.81 (0.73)	30.64 (2.79)	11206 (477)	0.74 (0.20)	0.22 (0.09)	0.56 (0.15)	0.37 (0.01)	Sub- M_{Ch}
SN 2021ucm	-16.1(3.2)	0.76 (0.12)	13.94 (3.50)	42.58 (2.98)	11137 (719)	1.41 (0.38)	0.12 (0.10)	1.05 (0.28)	0.70 (0.07)	Both
SN 2021wuf	-15.1(0.9)	0.72 (0.09)	12.33 (1.59)	35.09 (1.47)	12547 (2528)	1.21 (0.59)	0.12 (0.12)	1.14 (0.56)	0.56 (0.01)	Both
SN 2021yrf	-15.0(0.6)	0.55 (0.05)	11.91 (0.78)	37.27 (1.53)	11391 (1771)	1.13 (0.44)	0.11 (0.08)	0.88 (0.34)	0.52 (0.01)	Both
SN 2021ytp	-13.1 (0.8)	0.64 (0.06)	11.28 (1.08)	27.33 (1.69)	13894 (328)	0.90 (0.15)	0.15 (0.06)	1.04 (0.18)	0.56 (0.05)	Sub- M_{Ch}
SN 2022aaiq	-14.5(1.2)	0.49 (0.06)	9.02 (1.59)	53.29 (3.06)	9347 (349)	1.55 (0.29)	0.04 (0.02)	0.81 (0.15)	0.52 (0.01)	Near- $M_{\rm Ch}$
SN 2022fw	-16.4(0.6)	0.71 (0.07)	12.59 (1.26)	45.54 (2.11)	9551 (355)	1.18 (0.20)	0.10 (0.04)	0.65 (0.11)	0.69 (0.02)	Both
SN 2022 hrs	-15.3(0.2)	0.60 (0.05)	12.37 (0.35)	39.29 (1.31)	12349 (1257)	1.47 (0.40)	0.10 (0.04)	1.35 (0.36)	0.58 (0.01)	Both
SN 2022ydr	-13.9(1.0)	0.24 (0.05)	13.02 (1.28)	27.95 (1.60)	10010 (649)	0.49 (0.12)	0.27 (0.14)	0.29 (0.07)	0.19 (0.01)	Neither
SN 2022zut	-20.3(1.6)	0.61 (0.06)	15.14 (1.72)	47.88 (4.55)	11332 (497)	1.84 (0.51)	0.11 (0.06)	1.42 (0.39)	0.62 (0.03)	Near- $M_{\rm Ch}$
SN 2023bee	-17.1 (0.5)	0.82 (0.05)	13.25 (0.79)	45.14 (1.61)	11074 (829)	1.56 (0.35)	0.10 (0.04)	1.15 (0.25)	0.79 (0.02)	Near- $M_{\rm Ch}$

Note. The first 4 columns list the best-fit parameters given by Minim, then the expansion velocities, the ejecta masses, the calculated opacities, kinetic energies (see Section 5), nickel masses from the method of Khatami & Kasen (2019), and the consistency with near-Chandra and/or sub-Chandra explosion models are shown.

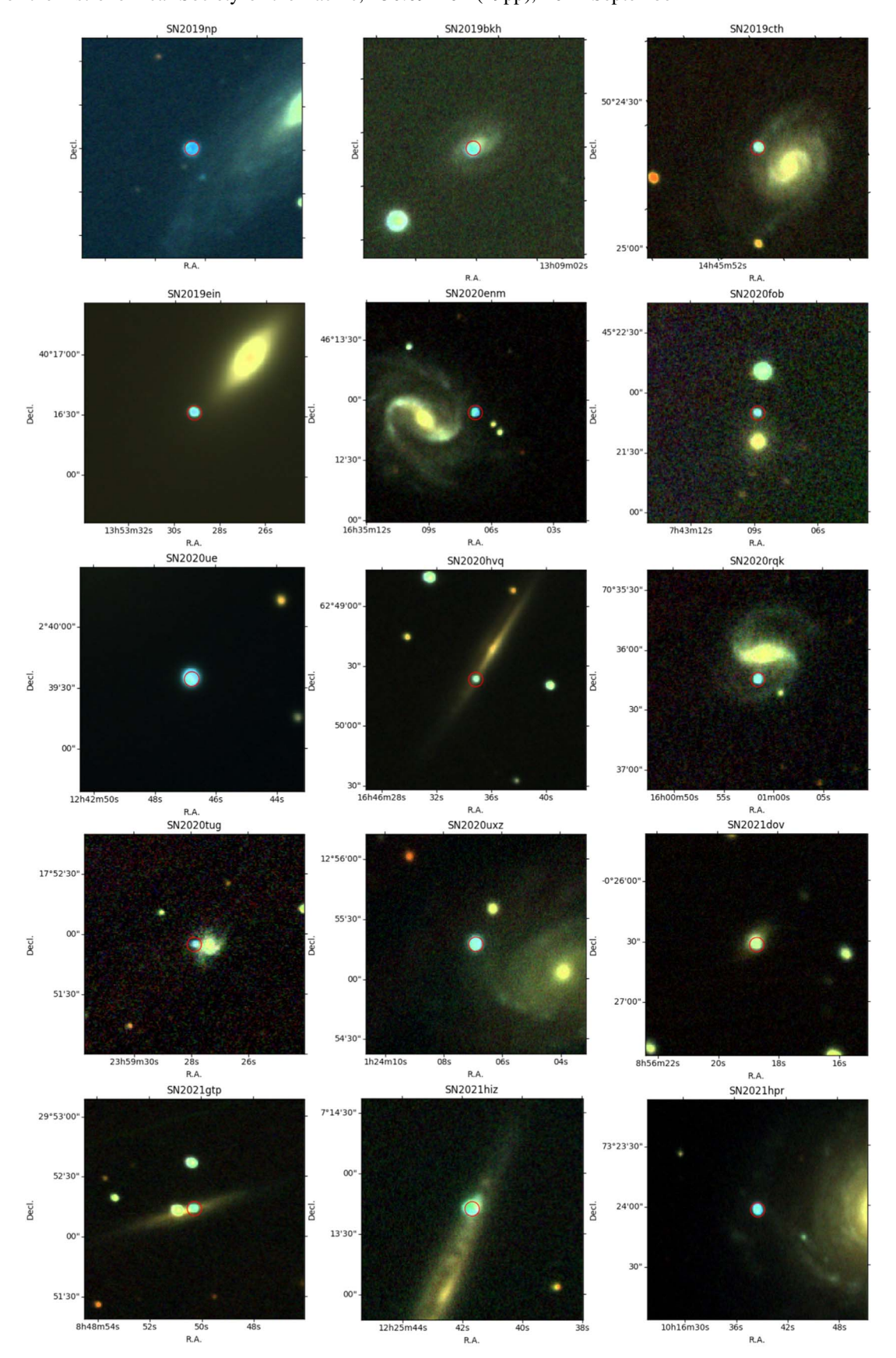


Figure 1. Color-combined *gri* images centered on the studied SNe. The size of each frame is 1.53×1.53 arcmin².

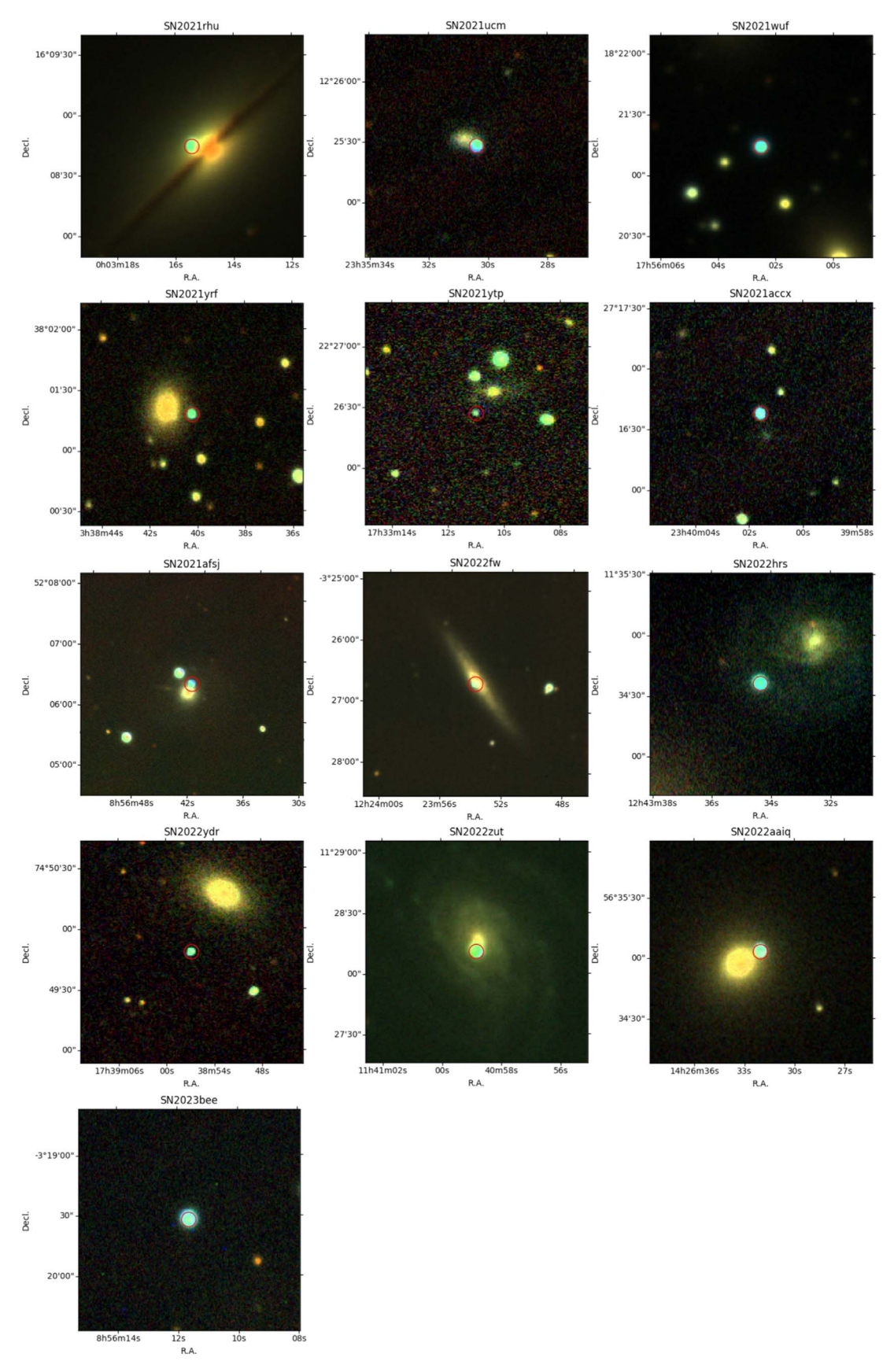


Figure 2. The same as Figure 1 but for additional SNe in the sample.

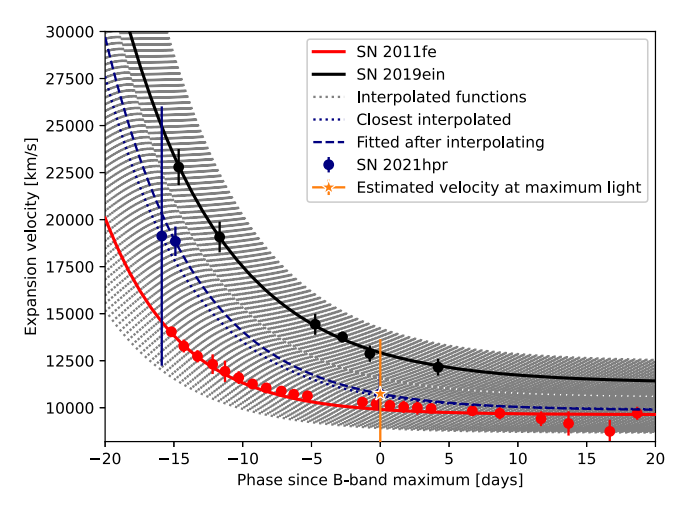


Figure 3. Visualization of the method we used to estimate v_{exp} for SN 2021hpr. The high- and low velocity bounds are defined by SN 2019ein (black symbols and thick curve) and SN 2011fe (red symbols and thick curve). Among the interpolated velocity curves (thin dotted curves) the best-fit curve for SN 2021hpr (blue dashed curve) is used to estimate the velocity at maximum (orange symbol).

from the Doppler shift of the Si II $\lambda 6355$ feature in the available spectra. For comparison, we also derived the physical parameters for the whole sample with the method of KTR20, i.e., without using spectroscopic velocities. After comparing the two sets of parameters taken with and without spectroscopic velocities, we found that the $v_{\rm exp}$ and $E_{\rm kin}$ parameters are significantly different. This is not surprising given the very approximate methodology used by KTR20 for estimating the velocities without spectroscopy. Thus, our new velocities and kinetic energies are more reliable than those obtained by KTR20 for their sample. Note also that Scalzo et al. (2019) revealed practically no correlation between their expansion velocities (inferred directly from the kinetic energy provided by explosion models) and $v_{Si II}$, thus, they concluded that $v_{Si II}$ is not a good proxy for estimating the kinetic energy of the bulk ejecta.

On the other hand, the ejecta masses ($M_{\rm ej}$), and opacities (κ) given by the two methods are in good agreement, as seen in Figure 6. We also compare the nickel masses and ejecta masses between our sample and that of KTR20 in Figure 7 (note that in Figure 6 the objects are the same, but the methods are different, while in Figure 7 we show the results of two different methods being applied to two different samples).

Figure 7 demonstrates that the two samples have similar distributions of both the ejecta masses and the nickel masses, even though different methods were applied to different samples. This shows that in spite of not using spectral information, the ejecta masses estimated by KTR20 are realistic, and their method is useful for estimating the ejecta mass in cases where getting near-maximum spectra is not

possible. It is important to note that in their analysis, KTR20 set an upper limit of $1.4\,M_\odot$ for the ejecta mass and a lower limit of $10,000\,\mathrm{km\,s^{-1}}$ for v_exp . Our method does not have these limits, so the distribution of ejecta masses can be wider, as seen in Figure 7. Other than that, we found good agreement between the two distributions: SNe in the KTR20 sample were found to have a mean M_ej of $\sim 1.07\,M_\odot$ and standard deviation of $0.15\,M_\odot$, which is consistent with those of our sample, $\sim 1.12\,M_\odot$ and $0.30\,M_\odot$, respectively.

6.2.3. Comparison with Scalzo et al. (2019)

Previously, ejecta masses for SNe Ia were also inferred by Scalzo et al. (2010, 2012), and Scalzo et al. (2014a). They used a method that was purely photometric, without any spectroscopic information, similar to KTR20. Their theoretical approach was based on a combination of several theoretical Ia explosion models, and they applied a different formalism than KTR20 and we did in the present paper. Scalzo et al. (2014a) estimated the ⁵⁶Ni and ejecta masses for their sample containing 19 SNe Ia, and concluded that about 50% of their sample SNe arose from the explosion of sub-Chandra WDs (see also Scalzo et al. 2014b). Their method was further applied on a larger sample (~45 SNe) and reached a similar conclusion (Scalzo et al. 2019).

Taking into account the uncertainties, 22 out of 27 SNe (81%) in our sample are consistent with sub-Chandra WD masses, but 13 of them are also consistent with both sub-Chandra and near-Chandra masses (see Table 3). This leaves 9 SNe (33%) in our sample whose ejecta masses are consistent with only sub-Chandra WDs. If we take the inferred ejecta masses at their face value, 11 out of 27 SNe (41%) fall within the mass range of sub-Chandra explosion, i.e., between 0.9 and $1.2\,M_{\odot}$. This is somewhat lower than the value found by Scalzo et al. (2019), but the uncertainties of the inferred ejecta masses, or the minor differences between the methodologies could explain the differences. Nevertheless, our results are consistent with the previous conclusions that a significant fraction (\sim 50%) of SNe Ia produce sub-Chandra ejecta masses after explosion.

6.3. Correlations between the Parameters

In this section we examine the correlation between the inferred physical parameters using p-values and Pearson correlation coefficients, which are presented in Figures 8, 9 and 12. In Figure 8 we show the correlation between the SALT3 x_1 parameter and the initial nickel mass (left panel) and the ejecta mass (right panel). The best-fitting linear equations are

$$M_{\text{Ni}} = 0.117(\pm 0.022) \cdot x_1 + 0.659(\pm 0.027),$$
 (6)

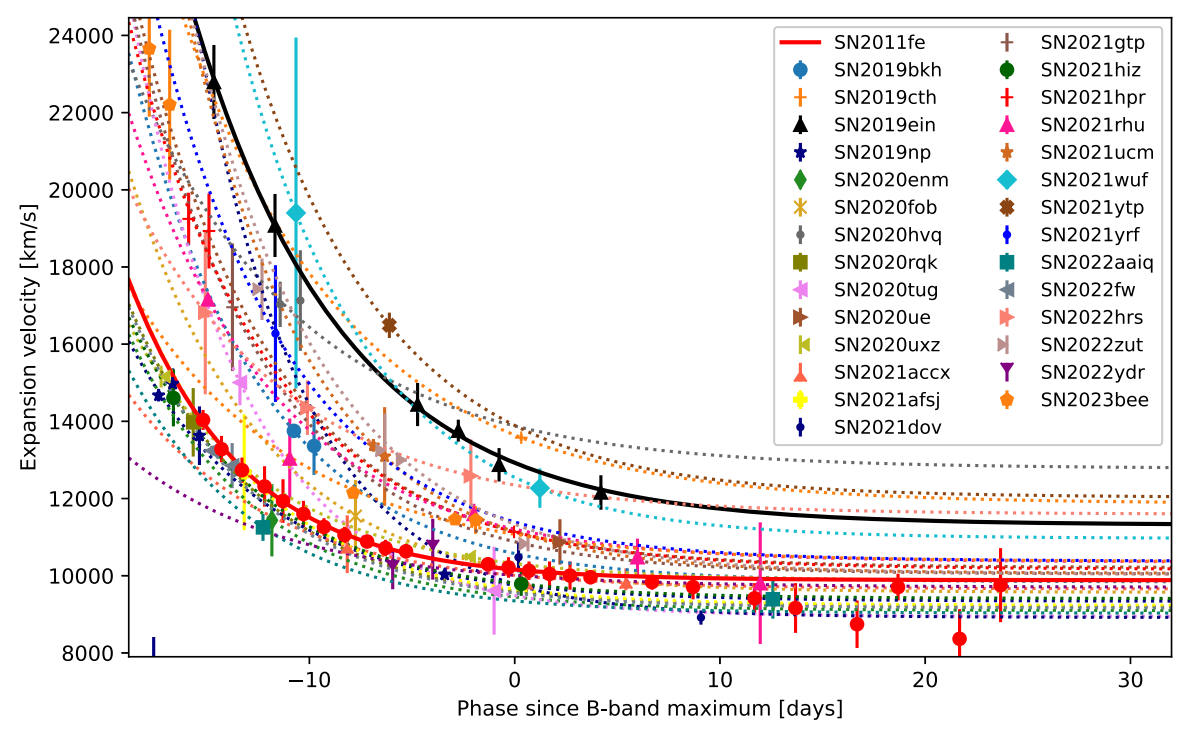


Figure 4. The expansion velocity evolution of the studied objects. Points represent the v_{exp} values determined from the Si II lines in the spectra, while dotted lines of the same color show the fitted exponential functions. Solid black and red curves show the fitted curves of SN 2019ein and SN 2011fe, respectively.

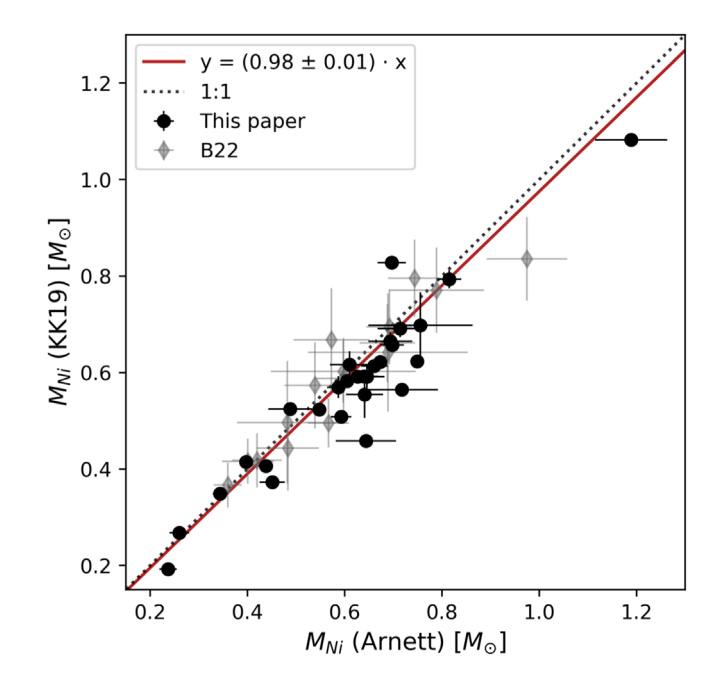


Figure 5. The comparison of the nickel masses estimated by fitting the bolometric light-curves with the Arnett-model (*x*-axis) to those calculated with the method of Khatami & Kasen (2019) (*y*-axis). Gray diamonds show the results by Bora et al. (2022), while SNe from the current sample are plotted with black circles. The solid red line indicates the linear relation fitted to all data, which is close to the 1:1 relation (shown by black dotted line).

and

$$M_{\rm ej} = 0.140(\pm 0.057) \cdot x_1 + 1.258(\pm 0.055).$$
 (7)

Both of these fittings agree well with those of Scalzo et al. (2019) within the errors, and show that the light curve decline rate (measured by the SALT3 x_1 parameter) correlates with the initial mass of the radioactive nickel synthesized in the explosion, as well as with the ejecta mass: lower decline rates (more positive x_1) correspond to higher $M_{\rm Ni}$ and $M_{\rm ej}$.

Similar correlation can be seen between $M_{\rm ej}$ and the timescale of the gamma-ray leakage (t_{γ}) , as shown in Figure 9 (left panel). This relation illustrates that in more massive ejecta it takes longer for the gamma-photons to diffuse out, therefore t_{γ} is a good indicator of progenitor mass (see also KTR20, but see Section 6.5 for caveats). The correlation with the expansion velocities (Figure 9 right panel) is weaker. From Equation (3), $M_{\rm ej} \approx v_{\rm exp}^2$ is expected, but, because of the presence of the $M_{\rm ej} \approx t_{\gamma}^2$ dependency, the correlation with the velocities looks smeared. In Figure 10 we show the relation between the ejecta mass and the optical opacity. The dotted line indicates the expected dependency from Equation (4) using the mean values for $t_{\rm LC}$ and $v_{\rm exp}$ (12.81 days and 10,929 km s⁻¹, respectively) inferred from our sample.

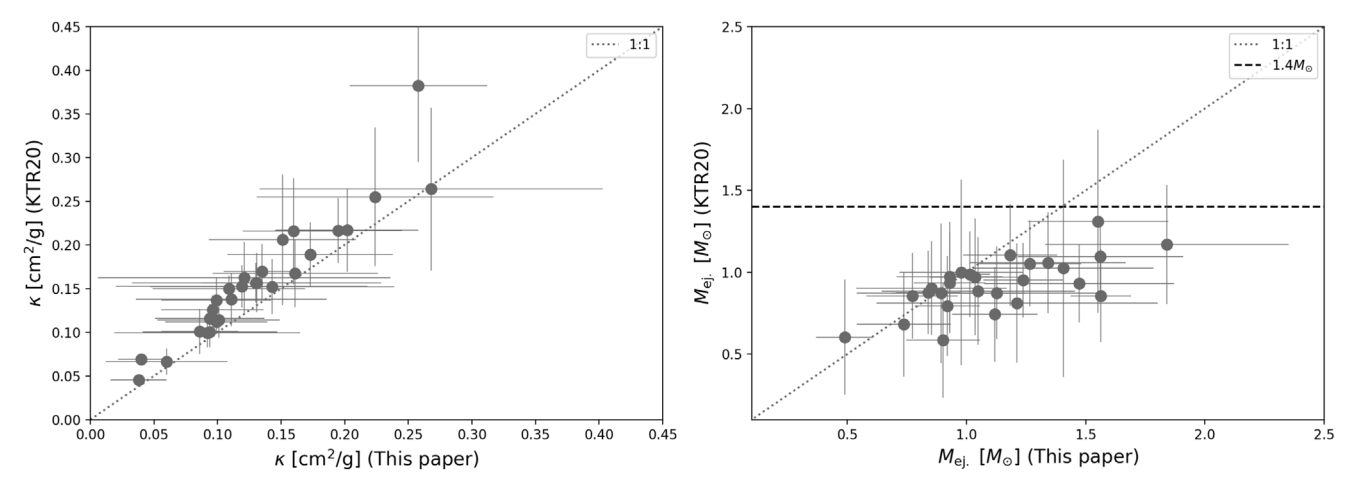


Figure 6. Comparison of ejecta opacities and masses with those obtained with the method of KTR20. 1:1 relations are shown with dotted lines, while the dashed line indicates the Chandrasekhar mass. Note that the method of KTR20 uses an assumption of $M_{\rm ej} \leq M_{\rm Ch}$, and this could be the cause for the deviation from the 1:1 relation in the $M_{\rm ej} > 1$ M_{\odot} mass range.

6.4. Comparison with Explosion Models

In this subsection we examine if our results are consistent with recently published explosion models.

First, we compare our estimated ejecta and nickel masses to the predictions of various detonation models in Figure 11. Here we show the relations predicted by He-shell double detonation models: the simulations by Gronow et al. (2021) (dotted line), the parameter survey of Polin et al. (2019) (dashed–dotted line), the hydrodynamic simulations of Fink et al. (2010) (dashed line), and the radiative transfer simulations of pure central detonations in sub- $M_{\rm Ch}$ carbon–oxygen WDs by Blondin et al. (2017) (solid line). We also compare our results with the predictions of the D⁶, TD (triple detonation), and QD (quadruple detonation) models of Tanikawa et al. (2019) (red solid line), and the delayed-detonation models of $M_{\rm Ch}$ WDs by Blondin et al. (2017) (red dotted line), and Seitenzahl et al. (2013) (red dashed line).

As Figure 11 illustrates, the majority of objects in our observational sample (22 out of 27) are consistent with the current sub- $M_{\rm Ch}$ models, including the thin He-shell double detonation models in SD progenitors. Even though some of the calculated ejecta masses are below $0.9 M_{\odot}$, which is the lowmass cutoff of the current sub-Chandra models that produce enough ⁵⁶Ni to be consistent with observed SNe Ia, the uncertainties of the inferred ejecta masses still make them consistent with the models (i.e., their difference from the cutoff mass is less than 1σ). Moreover, the DD models of Tanikawa et al. (2019), involving two merging WDs in a DD configuration, are also consistent with the observations, at least in the nickel mass range of $0.5-0.7 M_{\odot}$, but this is a bit uncertain since those models do not extend significantly below $\sim 1 \, M_{\odot}$ ejecta mass, unlike the SNe in our observational sample. The Tanikawa et al. (2019) models above $\sim 1 M_{\odot}$ are TD and QD explosions, where the companion WD also explodes, resulting in higher ejected masses. Overall, sub-Chandra detonations as well as DD models seem to be consistent with the majority of our observational sample.

There is only 1 object (the 91bg-like SN 2022ydr) that seems to be significantly below the cutoff mass, i.e., inconsistent with the current explosion models. Since all of these events are spectroscopically confirmed SNe Ia, this inconsistency is likely due to either some difficulties with the observations, or the failure of the Arnett-model for this particular object (see Section 6.5).

On the other hand, Figure 11 shows that more than 50% of the SNe (17 out of 27) also fall within the mass range of near-Chandra DDC models $(1.2 \leq M_{\rm ej} \leq 1.5 \, M_{\odot})$ if their errorbars are taken into account. However, only 4 of them exceed $1.2 \, M_{\odot}$ significantly, as the others have uncertainties that extend below $1.2 \, M_{\odot}$. The near-Chandra models, plotted with red dashed and dotted lines in Figure 11, have the same $M_{\rm ej} \approx 1.44 \, M_{\odot}$ in general, and they show practically no correlation between their $M_{\rm ei}$ and $M_{\rm Ni}$.

It is important to note that due to the uncertainties of the calculated ejecta masses, a significant fraction of our sample (13/27, 48%) are consistent with both the near-Chandra and sub-Chandra explosion scenarios, so it is not possible to distinguish between these two possibilities in those cases.

These fractions can also be estimated using the Gaussian Probability Density Function (PDF) shown in the bottom panel of Figure 7. Integrating the PDF below $0.9\,M_{\odot}$, between $0.9\,$ and $1.2\,M_{\odot}$, between $1.2\,$ and $1.5\,M_{\odot}$ and above $1.5\,M_{\odot}$, corresponding to below-sub-Chandra, sub-Chandra, near-Chandra and super-Chandra mass regimes, respectively, we got the probabilities for these regimes as 0.32, 0.33, 0.20, and 0.15, respectively. These are also indicated in the legend of

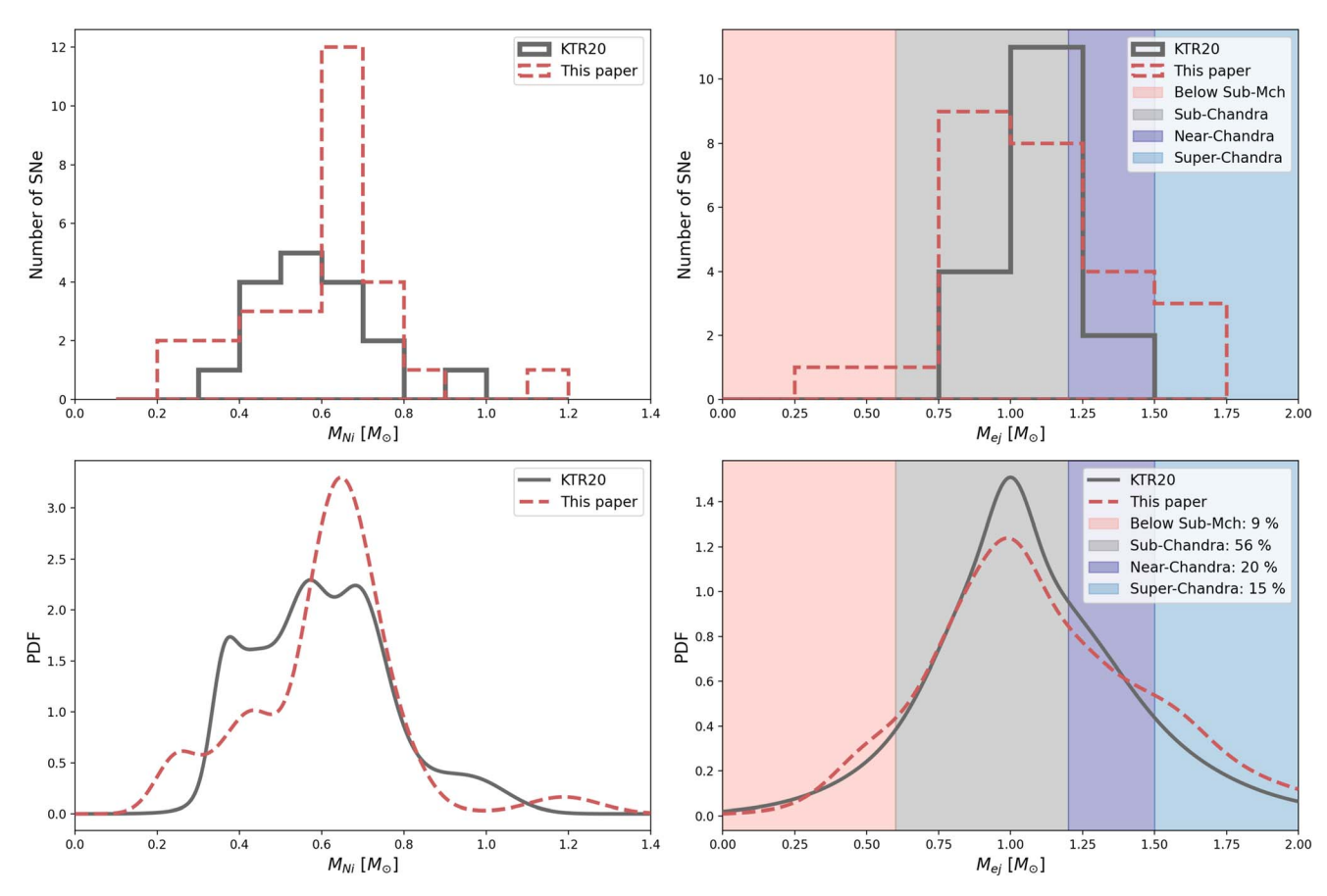


Figure 7. Top panels: comparison of the histograms of the nickel and ejecta mass distributions of our sample (red) with that of KTR20 (gray). Bottom panels: the sums of individual Gaussian distributions of the nickel and ejecta masses with their errors taken into account as widths of the individual Gaussians. The colored background in the right panels codes the different mass regimes for super-Chandra ($M_{\rm ej} > 1.5~M_{\odot}$), near-Chandra ($1.2~M_{\odot} < M_{\rm ej} < 1.5~M_{\odot}$), sub-Chandra ($0.9~M_{\odot} < M_{\rm ej} < 1.2~M_{\odot}$) and below sub-Chandra ($0.9~M_{\odot} < 0.9~M_{\odot}$) ejecta masses.

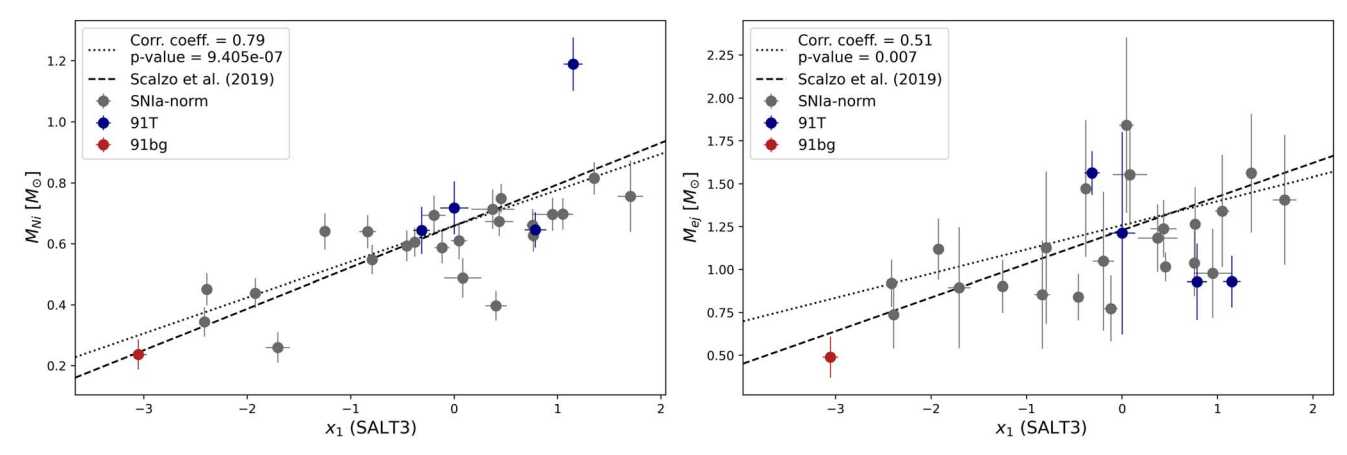


Figure 8. Nickel mass (left) and ejecta mass (right) plotted against the SALT3 x_1 parameter. The relations determined by Scalzo et al. (2019) are shown with dashed lines, while dotted lines present the relations fitted by us. 91T-like SNe are marked with blue dots, while gray and red symbols denote the normal and 91bg-like SNe, respectively.

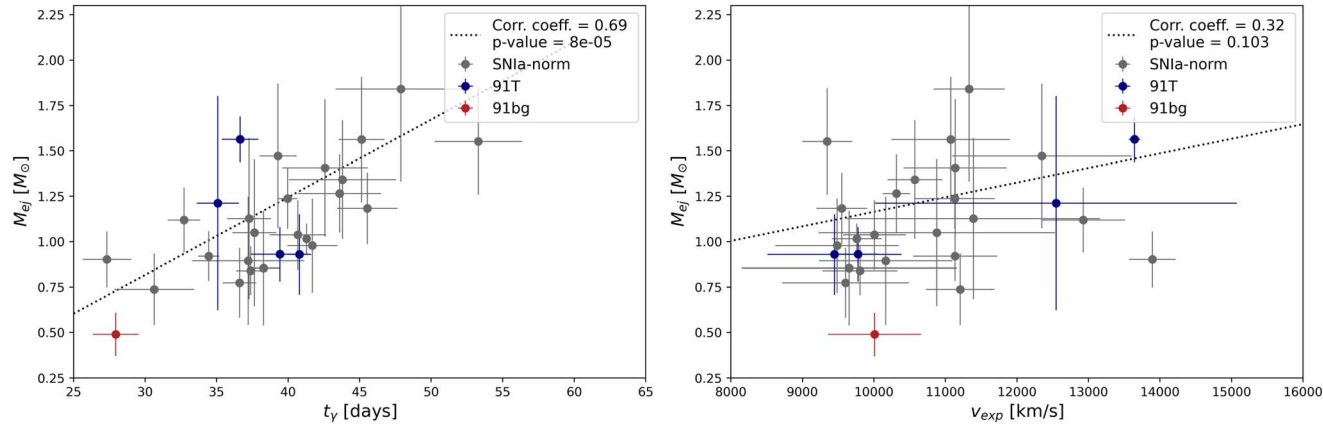


Figure 9. Ejecta masses plotted against gamma-ray timescales (left) and expansion velocities (right) for all observed SNe. The dotted lines show the relations fitted by us, blue dots mark the 91T subtypes, gray dots the normal SNe Ia, and red dots show the 91bg subtypes.

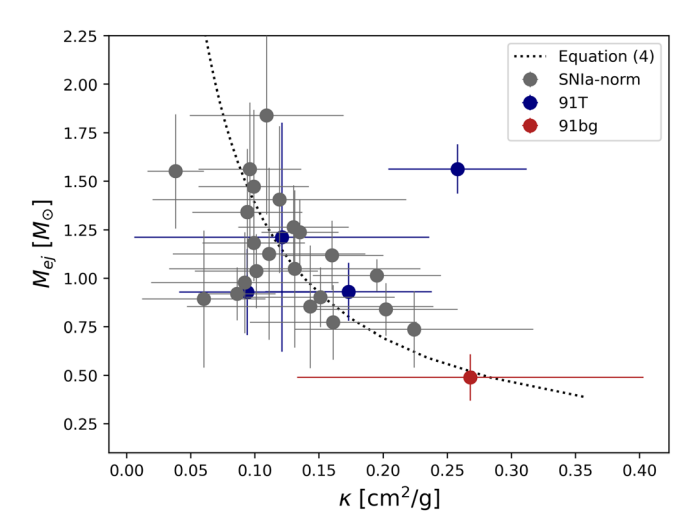


Figure 10. Ejecta masses plotted against the optical opacity κ . The dotted line shows the prediction by Equation (4), blue dots mark the 91T subtypes, gray dots the normal SNe-Ia, and red dots show the 91bg subtypes.

Figure 7. Again, since the uncertainties seem to be higher than the mass difference between the sub-Chandra, and near-Chandra channels, it is difficult to draw a definite conclusion, but it seems to be slightly more probable (at least in the present sample) that a SN belongs to the sub-Chandra mass regime instead of being a near-Chandra event.

As seen in Figure 11, the range of the inferred Ni-masses is fully consistent with the ones predicted by both the near-Chandra and sub-Chandra models. For the former, where the ejecta masses are the same ($M_{\rm Ch}$), the differences in the Ni-masses can be achieved by the number of ignition sparks and the implementation of the deflagration-to-detonation transition (e.g., Seitenzahl et al. 2013). On the contrary, in sub-Chandra explosions the synthesized Ni-mass is connected with the mass of the WD (and partly with the details of the ignition

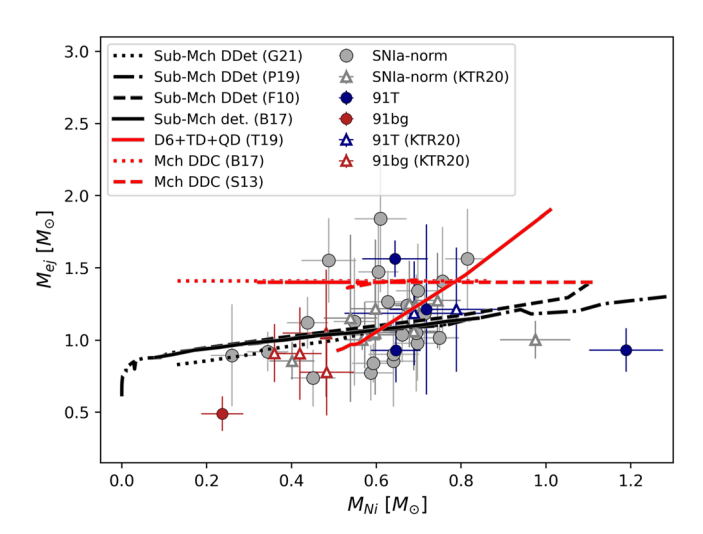


Figure 11. Comparison of the distribution of the observed SNe on the $M_{\rm Ni}$ – $M_{\rm ej}$ diagram with the predictions of various explosion models (Fink et al. 2010; Seitenzahl et al. 2013; Blondin et al. 2017; Polin et al. 2019; Tanikawa et al. 2019; Gronow et al. 2021). The blue, gray and red colors code the 91T-, normal- and 91bg subtypes respectively. SNe from this paper are plotted with filled circles, while hollow circles represent the objects from KTR20.

mechanism), which is reflected by the slope of the lines representing the sub-Chandra models in Figure 11. The fact that most of the inferred ejecta masses also seem to show a similar trend suggests that those SNe (or at least some of them) might also be produced by sub-Chandra explosions, but the uncertainties of the inferred ejecta masses prevent making a definite conclusion at the moment.

In Figure 12 we plot the correlation between the inferred bolometric luminosity and the reddening-corrected $(B-V)_0$ color at the moment of maximum light. We compare these data with the results of two explosion models given by Blondin et al. (2017): we plot the results of the central detonation sub-

Chandra scenario with a dotted curve, while the dashed curve shows the same from the Chandrasekhar-mass delayed-detonation model. It can be seen that the models follow the observed trend of most SNe Ia having $(B-V)_0\approx 0.0$ mag around maximum, with the fainter events being redder. However, considering just the luminosity and the color at the moment of maximum is not enough to differentiate between these two explosion scenarios, as they both fit our observed sample relatively well. Our observations also show brighter and bluer events than those predicted by the Blondin et al. (2017) models.

Overall, we conclude that the predictions of current sub-Chandra models are consistent with the ejecta and nickel masses measured from observations for most SNe Ia in our sample. Due to the uncertainties of the inferred masses, the conventional delayed-detonation models are also compatible with many of the SNe in our sample, but those models have difficulties explaining the significant number of sub-Chandra ejecta masses.

6.5. Concerns and Caveats Regarding the Methodology

The Arnett-model as well as similar semi-analytic LC models have been widely used for inferring ejecta parameters of various types of SNe, even though such a model is (of course) far from being perfect, and suffers from several issues. Regarding the ejecta mass, one of the most serious, well-known issues is the degeneracy between $M_{\rm ej}$ and the optical opacity κ , as seen in Equation (4): from the t_{LC} timescale, representing the pre-maximum part of the LC, both κ and $v_{\rm exp}$ must also be known to calculate M_{ej} . κ , however, is treated very approximately within the framework of the Arnett-model: it is assumed to be constant both in space (within the ejecta) and in time (i.e., no evolution), neither of which is expected to be true in reality. Thus, κ should be considered only as a technical, rather than a self-consistent physical parameter, which characterizes the timescale of the diffusion of photons within a spherical, constant-density, homologously expanding ejecta.

Despite this well-known caveat, it is somewhat surprising that applying physically motivated estimates for κ , like the expected Thompson-scattering opacity of a metal-dominated plasma ($\kappa \sim 0.1~{\rm cm^2~g^{-1}}$), one can get quite reasonable ejecta mass estimates for SNe Ia from observationally inferred $t_{\rm LC}$ parameters. In order to verify this statement using the present sample, we explored two alternative ways in deriving the ejecta masses. As a first experiment, we calculated ejecta masses from Equation (4) assuming $\kappa = 0.1~{\rm cm^2~g^{-1}}$ and $v_{\rm exp} = 10,000~{\rm km~s^{-1}}$. Second, we substituted $v_{\rm exp}$ into Equation (3) with the kinetic energy $E_{\rm kin}$ taken from Equation (5), expressed $M_{\rm ej}$, and assumed $E_{\rm kin} = 10^{51}~{\rm erg}$ as a uniform value for the whole sample. The results of these experiments are plotted as histograms and Gaussian PDFs in Figure 13, together with the distribution of the original $M_{\rm ej}$ values listed in Table 3.

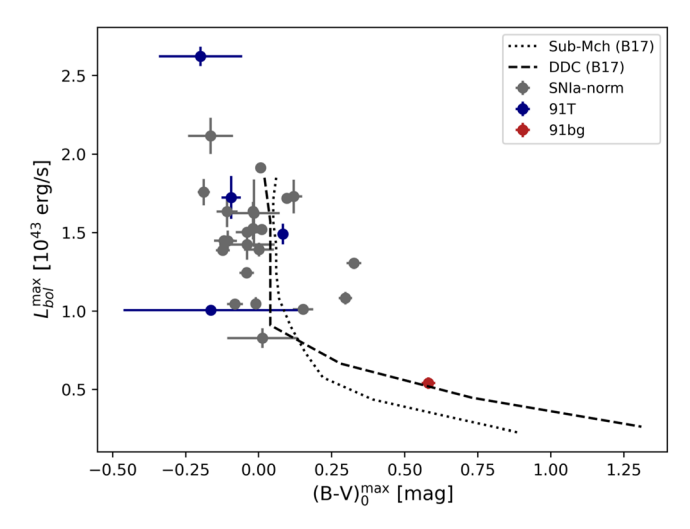


Figure 12. The peak bolometric luminosity against the $(B-V)_0$ color at the moment of maximum. We compare the data with the sub-Chandra detonation (dotted curve) and Chandrasekhar-mass delayed detonation (dashed curve) models of Blondin et al. (2017). The blue, gray and red markers show the 91T-, normal- and 91bg subtypes, respectively.

It is seen that, despite the over-simplifying assumptions used in these experiments, either the constant opacity and expansion velocity, or the kinetic energy that are uniform for the whole Ia sample, the resulting ejecta masses are close to the ones estimated from the gamma-ray leaking timescales, even though the peaks of their distributions are shifted to somewhat higher values. The mean ejecta mass from the uniform opacity assumption is $\langle M_{\rm ej} \rangle = 1.32 \, M_{\odot}$ with a standard deviation of $0.47 M_{\odot}$, while from the uniform kinetic energy assumption these are $\langle M_{\rm ej} \rangle = 1.26 \, M_{\odot}$ and $0.18 \, M_{\odot}$. It is seen that using such kind of physically motivated assumptions one can get slightly different ejecta masses than by using the data-driven method we preferred in this paper, which makes as minimal assumptions as possible within the framework of the Arnettmodel. Still, even if we adopted any of the results from the above experiments, a non-negligible fraction of the sample $(\sim 7\%$ in the uniform opacity model, or $\sim 19\%$ in the uniform kinetic energy model) would be consistent only with sub-Chandra explosions (see Table 4). However, the uniform opacity model would also predict that $\sim 26\%$ of the sample is consistent only with near-Chandra explosions, with \sim 22% of the sample being super-Chandra ($M_{\rm ej} > 1.5 \, M_{\odot}$). In the fixed kinetic energy model the fraction of only near-Chandra explosions is higher ($\sim 30\%$). The number of SNe that are consistent with both explosion channels are nearly the same (40%–50%), regardless of the adopted LC interpretation. Thus, it seems that the Arnett-models that relate the timescales of the SN bolometric LCs to the basic physical parameters of the ejecta are consistent with the observations only if a fraction of the observed SNe Ia are produced by sub-Chandra progenitors.

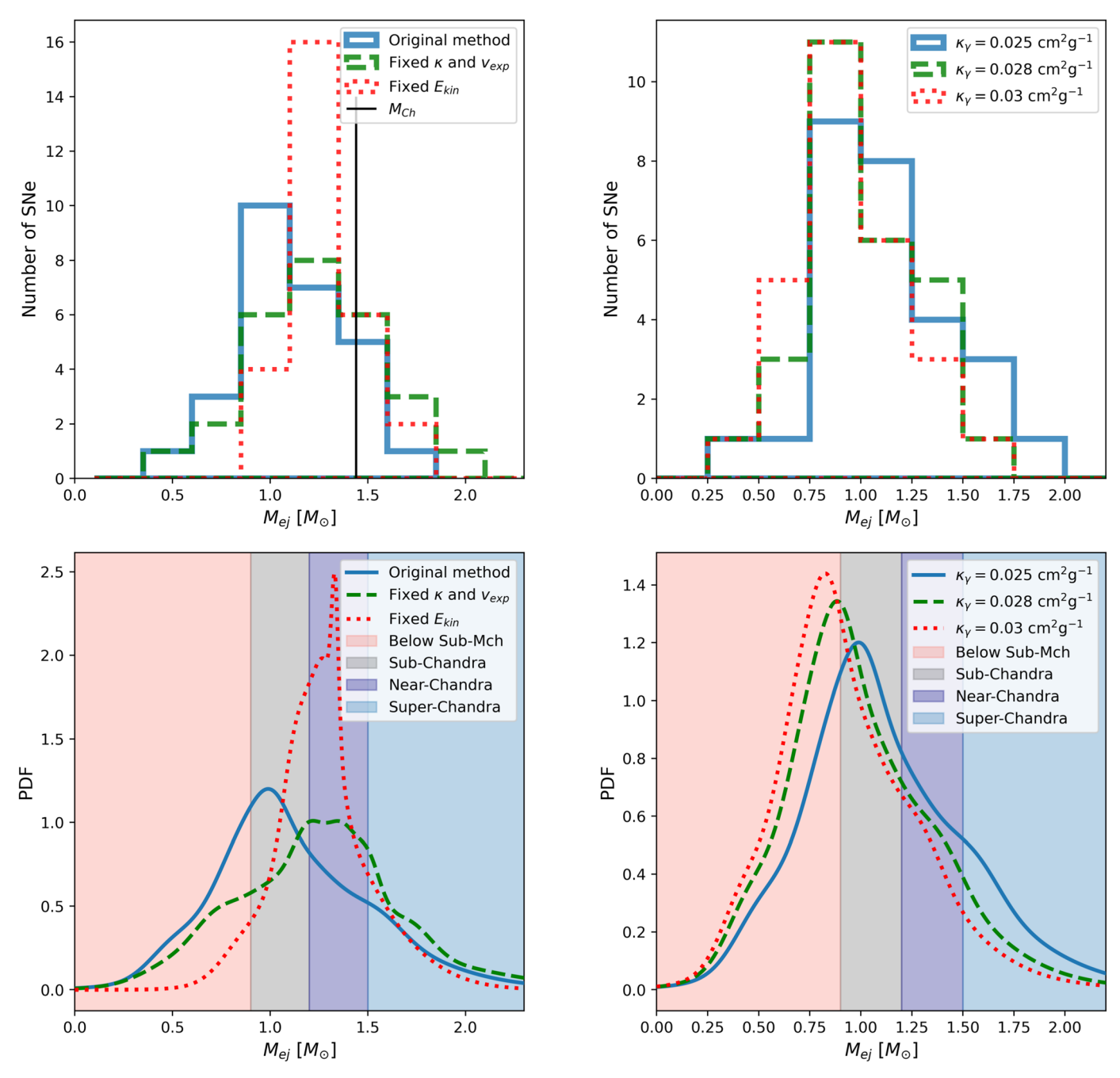


Figure 13. Top panel: histogram of ejecta masses listed in Table 3 (blue), masses inferred from Equation (4) assuming uniform opacity (green), and from Equation (3) assuming uniform $E_{\rm kin}$ (red). The black vertical line indicates the Chandrasekhar-mass. Bottom panel: sum of Gaussian distributions for the same ejecta masses as in the top panel. The background is color-coded by the same mass ranges as in Figure 7.

Figure 14. Top panel: histograms of the ejecta masses inferred from Equation (3) assuming different κ_{γ} values. We show the ejecta masses obtained with $\kappa_{\gamma} = 0.025 \text{ cm}^2 \text{ g}^{-1}$ (solid blue), $\kappa_{\gamma} = 0.028 \text{ cm}^2 \text{ g}^{-1}$ (dashed green), and $\kappa_{\gamma} = 0.03 \text{ cm}^2 \text{ g}^{-1}$ (dotted red). Bottom panel: Gaussian distributions of the different masses, constructed the same way as in Figure 7.

While discussing the physics of SNe Ia, Livio & Mazzali (2018) argued that ejecta mass estimates based on the Arnett-model are sensitive only to the opaque mass. Since the optical opacity is mostly sensitive to the Fe-group elements, such a

method can recover only the mass rich of Fe-group elements. They concluded that "It would therefore not be surprising for Scalzo et al. to find masses that are proportional to the nickel mass." This argument, however, assumes that the ejecta mass

Companion of the bumple 51 to 11 th 21 problem 11 to 25 and of the 11 th								
Method	$\langle M_{ m ej} angle$	$\sigma(M_{ m ej})$	Consistent only with Sub- $M_{\rm Ch}$	Consistent only with near- $M_{\rm Ch}$	Consistent with Both	Outside of Both Channels		
Fixed κ , $v_{\rm exp}$	1.32	0.47	7%	26%	44%	22%		
Fixed E_{kin}	1.26	0.18	19%	30%	52%	0%		
$\kappa_{\gamma} = 0.025 \text{ cm}^2 \text{ g}^{-1}$	1.12	0.30	33%	15%	48%	4%		
$\kappa_{\gamma} = 0.028 \text{ cm}^2 \text{ g}^{-1}$	0.99	0.27	37%	4%	44%	15%		
$\kappa_{\gamma} = 0.030 \text{ cm}^2 \text{ g}^{-1}$	0.93	0.25	33%	0%	41%	26%		

Table 4

Comparison of the Sample SNe with Explosion Models Based on the Inferred Ejecta Masses

Note. First column: method for calculating M_{ej} . 2nd and 3rd columns: the mean and the standard deviation of the masses inferred by each method. Next columns: the percentage of SNe that are consistent with only sub-Chandra, only near-Chandra, both or neither explosion models. See Section 6.5 for explanation.

estimate is based on the optical (average) opacity, like in Equation (4). It is emphasized that the ejecta mass estimates that are based on the gamma-ray transparency timescale (t_{γ}) that we use in this paper (and also the numerous previous studies discussed in Section 6), is much less affected by the uncertainty of the gamma-ray opacity, κ_{γ} , which is constrained much better and it is less sensitive to the actual chemical composition of the ejecta than the optical opacity.

In this study we have adopted $\kappa_{\gamma} = 0.025 \, \mathrm{cm}^2 \, \mathrm{g}^{-1}$ from Guttman et al. (2024), who derived the value from a semi-analytic method. Some previous works used $\kappa_{\gamma} = 0.03 \, \mathrm{cm}^2 \, \mathrm{g}^{-1}$ from Wheeler et al. (2015) but this value goes back to Colgate et al. (1980) who inferred $\kappa_{\gamma} = 0.028 \, \mathrm{cm}^2 \, \mathrm{g}^{-1}$ using a multiple-scattering Monte Carlo gamma-ray transport code developed at Los Alamos. It is seen that these values are in good agreement with each other. Still, because κ_{γ} appears in the denominator in Equation (3), the inferred $M_{\rm ej}$ masses are sensitive to the adopted value of this parameter. In order to test the effect of the adopted gamma-ray opacity on the final results, we have recalculated the ejecta masses from Equation (3) using $\kappa_{\gamma} = 0.028$ and $0.03 \, \mathrm{cm}^2 \, \mathrm{g}^{-1}$.

The results are shown in Figure 14, where the histograms and PDFs of the inferred $M_{\rm ej}$ values corresponding to the different adopted gamma-ray opacities are plotted together. It is seen that adopting a slightly higher gamma-ray opacity decreases the inferred ejecta masses (Table 4), as expected. This can be considered as a systematic uncertainty of the calculated ejecta masses. However, the range of the potential gamma-ray opacity values is small enough that this systematic uncertainty is not severe. Indeed, as Table 4 shows, adopting $\kappa_{\gamma} = 0.03 \text{ cm}^2 \text{ g}^{-1}$ would decrease only the number of systems that are consistent only with the near-Chandra scenario, but the fraction of sub-Chandra SNe would be nearly the same. It is true, however, that the higher gamma-ray opacity would significantly increase the fraction of SNe that have too low ejecta masses, hence they would become inconsistent even with the sub-Chandra explosion models. Still, regardless of the adopted gamma-ray opacity value, the majority of the SNe in our sample are consistent with both explosion channels.

These calculations confirm that the ejecta masses inferred from the gamma-ray transparency timescales measured at late phases suggest that more SNe Ia may be due to sub-Chandra explosions than what could be estimated from the near-maximum LCs. The key parameter behind this conclusion is clearly the gamma-ray opacity, which is much better constrained than the optical (electron scattering) opacity.

The expansion velocity parameter, $v_{\rm exp}$, is also problematic. In the original paper Arnett (1982) used the term "scaling velocity," $v_{\rm sc}$, to emphasize that it is more like a parameter describing the homologous expansion of a constant-density sphere instead of being an actually observed velocity. However, he also argued that "... if we take $v_{\rm sc}$ from the photospheric fluid velocity near maximum light, this value is not far from the uniform-density estimate." This note was the main motivation for us to assign the observed $v_{\rm Si\ II}$ at maximum to the expansion velocity in our calculations.

In order to test whether the observed $v_{\rm Si~II}$ velocities were valid expansion velocities in the Arnett-model, we inferred the expected expansion velocity as a function of t_{γ} from Equation (3) by assuming a fixed ejecta mass, and compared them with the observed velocities (see Figure 15). It is seen that most of the observed points fall within the two theoretical curves corresponding to $M_{\rm ej}=0.9$ and $1.5\,M_{\odot}$. Thus, using the observed $v_{\rm Si~II}$ velocity and t_{γ} values one can get reasonable estimates for the ejecta mass via Equation (3).

Still, the question remains whether $v_{\rm Si~II}$ gave the *total* ejecta mass when inserting it into Equation (3). In other words: is it possible that $v_{\rm Si~II}$ probes only the inner, optically thick part of the ejecta at the moment of maximum light, resulting in a mass that is systematically lower than the true $M_{\rm ej}$? This is a nontrivial problem, because the Arnett-model assumes a constant density ejecta, while real SNe Ia have different density profiles. The detailed investigation of this issue will be the subject of a subsequent paper (J. Vinkó et al. 2024, in preparation), but a quick analytic estimate is given here. Following Magee et al. (2020), we used the exponential density profile of a fiducial SN Ia having $M_{\rm ej} = 1.44 \, M_{\odot}$ and $E_{\rm kin} = 10^{51}$ erg to calculate the velocity at the photosphere via the usual condition of

 $\tau(\nu_{\rm ph})=2/3$, where $\tau(\nu_{\rm ph})$ is the optical depth of the ejecta at $\nu_{\rm ph}$. After that, the mass above $\nu_{\rm ph}$, which is optically thin and may not contribute to the photon diffusion, was determined by integrating the density profile between $\nu_{\rm ph}$ and $\nu_{\rm max}=30,000~{\rm km\,s^{-1}}$ (Magee et al. 2020). Adopting $t_{\rm max}\approx 18~{\rm days}$ as the moment of maximum light after explosion, we got $\nu_{\rm ph}=11,571~{\rm km\,s^{-1}}$ and $13,238~{\rm km\,s^{-1}}$ for $\kappa=0.1$ and $0.2~{\rm cm^2\,g^{-1}}$, respectively. The masses above these photospheric velocities are $\Delta M_{\rm ej}\approx 0.20$ and $0.13~M_{\odot}$, respectively. It is seen that even though the mass probed by the Arnett-model is $1.44-0.20=1.24~M_{\odot}$, i.e., $\sim 14\%$ lower than $M_{\rm Ch}$, it would still be within the range of the near-Chandra explosions. Thus, it is not likely that the significant fraction of the sub-Chandra ejecta masses given by the Arnett-model are simply due to the systematically low velocities inserted into Equation (3).

Yet another important restriction of the Arnett-model is the assumption of a centrally localized heating source, i.e., the spatial distribution of ⁵⁶Ni is strongly peaked at the center. This may be a fair assumption for a fiducial SN Ia model having $M_{\rm Ch}$ mass and $\sim 0.6\,M_{\odot}$ (i.e., $\sim 40\%$ mass fraction) of $^{56}{\rm Ni}$. However, it can be expected to break down in several cases: (i) when $M_{\rm Ni} \gtrsim 1.0 \, M_{\odot}$, i.e., the majority of the ejecta mass consists of radioactive Ni, (ii) when $M_{\rm ej} \ll M_{\rm Ch}$, i.e., for sub-Chandra explosions, and (iii) when ⁵⁶Ni has a more extended distribution for other reasons, e.g., off-center ignition (Seitenzahl et al. 2013; Magee et al. 2020). If the radioactive heating is not centrally localized, the photon diffusion timescale may get shorter, and some of the gamma-rays produced by the radioactive decay may start to leak out from the expanding ejecta earlier than expected for a centrally located heating source. These effects may result in shorter t_{LC} and t_{γ} timescales for the observed light curve, which, in the formalism of the Arnett-model, gives an ejecta mass that is lower than in reality.

This caveat may explain the presence of SNe having ejecta masses significantly less than the lower limit of sub-Chandra Ia models $(0.9\,M_\odot)$, which otherwise have "normal" nickel masses in the observed sample (Figure 11). This may also be the explanation for those objects having $M_{\rm Ni}\gtrsim M_{\rm ej}$ (SN 2021dov or SN 2017erp in KTR20). Since it is certainly a limitation for the applicability of the Arnett-model to real data, the resulting too low ejecta masses or the cases when $M_{\rm Ni}/M_{\rm ej}\approx 1$ should be treated with caution.

Even though these undeniable caveats exist, we believe that radiation-diffusion (Arnett-) models can still give us reliable constraints on the global physical properties of SNe Ia if the photometry extends well beyond maximum light into the regime when the ejecta becomes semi-transparent to gammarays, and there is near-maximum spectroscopy available.

7. Summary

We presented multicolor photometry of 28 nearby Type Ia supernovae taken during the first 4 yr of operation of the RC80

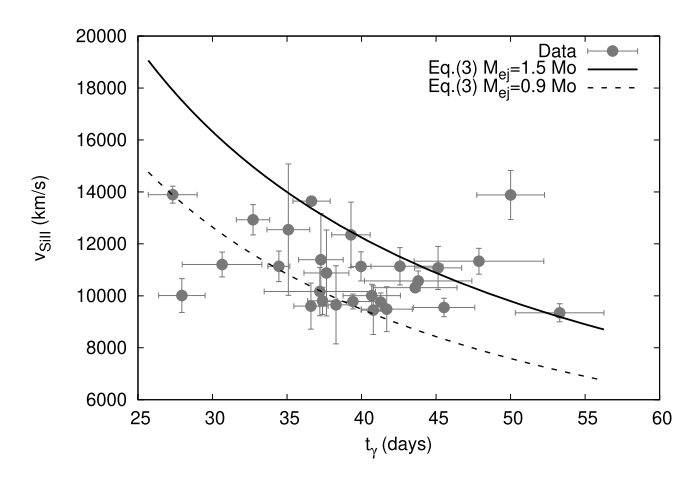


Figure 15. Observed $v_{\text{Si II}}$ velocities (filled symbols) compared with the expansion velocities for fixed ejecta masses against the gamma-ray leaking timescale t_{γ} . The fixed ejecta masses corresponding to the continuous and dashed curves are shown in the legend.

and BRC80 telescopes at Piszkéstető station of Konkoly Observatory and Baja Observatory of University of Szeged, Hungary. Using the multicolor light curve fitting codes SALT3 and MLCS2k2, we determined luminosity distances as well as total dust extinctions to the sample SNe, which we used to construct their pseudo-bolometric LCs. Fitting the bolometric LCs with the Arnett-model yielded the mass of the radioactive nickel synthesized during the explosion along with the important timescales of $t_{\rm LC}$, and t_{γ} , which can be used to estimate the ejecta mass if the photospheric velocity is known. After collecting previously unpublished optical spectra taken by LCO telescopes and the HET, supplemented by public spectra downloaded from the TNS, we measured the velocities of the Si II λ 6355 feature and determined the $v_{\rm Si~II}$ velocities at the moment of maximum for all of our sample SNe.

Via Equations (3)–(5) we calculated the ejecta masses, optical opacities and kinetic energies for the sample SNe. We found that based on the inferred ejecta masses, ~48% of the sample SNe are consistent with both sub-Chandra and near-Chandra explosion models. Our results suggest that \sim 33% of the sample can be explained by only sub-Chandra progenitors. This is a somewhat lower value than appeared earlier in the literature (Scalzo et al. 2014a, 2014b, 2019; Könyves-Tóth et al. 2020; Liu et al. 2023b), but together with the events that are consistent with both explosion channels, this could be as high as 81%. The fraction of near-Chandra events was found to be in between $\sim 15\%$ and 63%, but this estimate may suffer from low-number statistics and can also be affected by the adopted value of the gamma-ray opacity. If we used $\kappa_{\gamma} = 0.03 \text{ cm}^2 \text{ g}^{-1}$ instead of 0.025, the maximum fraction of near-Chandra SNe Ia would decrease down from 63% to $\sim 41\%$ at best.

After comparing our results with multiple types of recent explosion models, we revealed that significant differences between the predictions of near-Chandra and sub-Chandra models cannot be seen in the color-luminosity relation around maximum (see Figure 12). We showed that the ejecta mass can be a useful constraint to confront the predictions of various explosion models with the observations. From the results presented in this paper it seems that the majority of the studied SNe Ia are consistent with either the sub-Chandra or the near-Chandra explosion models, but the accuracy of the current photometric mass estimates are not high enough to clearly distinguish between these two possibilities.

Acknowledgments

We thank the anonymous referee for their helpful comments and guidance in improving our paper.

This research is supported by NKFIH-OTKA grants K-142534, K-134432, K-138962, FK-134432, and PD-134784, NKFIH Élvonal grant KKP-143986, and NKFIH excellence grant TKP2021-NKTA-64 from the National Research, Development and Innovation Office (NKFIH), Hungary. The RC80 and BRC80 telescopes have been supported by the GINOP 2.3.2-15-2016-00033 project from the Government of Hungary, funded by the European Union. J.C.W. and J.V. are supported by NSF grant AST-1813825. Á. S., C.K., and A.B. acknowledge financial support of the KKP-137523 "SeismoLab" Élvonal grant of NKFIH, Hungary. B.C. received support from the Lendület Program LP2023-10 of the Hungarian Academy of Sciences. K.V. and L.K. are supported by the Bolyai János Research Scholarship of the Hungarian Academy of Sciences. Financial support from the Austrian-Hungarian Action Foundation grants 112öu1 is also acknowledged. Z.B. is supported by the ÚNKP-22-2 New National Excellence Program of the Ministry for Culture and Innovation from the source of the National Research, Development and Innovation Fund. V.V. is supported by the ÚNKP-22-1 New National Excellence Program of the Ministry for Culture and Innovation from the source of the National Research, Development and Innovation Fund. Z.B., Á.H.-D., N.O.S., and V.V. thank the financial support provided by the undergraduate research assistant program of Konkoly Observatory. L.K. acknowledges the Hungarian National Research,

Development and Innovation Office grant OTKA PD-134784. Zs.M.Sz. acknowledges funding from a St Leonards scholar-ship from the University of St Andrews, and is a member of the International Max Planck Research School (IMPRS) for Astronomy and Astrophysics at the Universities of Bonn and Cologne. K.A.B. is supported by an LSST-DA Catalyst Fellowship; this publication was thus made possible through the support of grant 62192 from the John Templeton Foundation to LSST-DA. A.V.F. is grateful for financial assistance from the Christopher R. Redlich Fund and many other donors.

This work makes use of data from the Las Cumbres Observatory global telescope network. The LCO group is supported by NSF grants AST-1911151 and AST-1911225.

The HET is a joint project of the University of Texas at Austin, the Pennsylvania State University, Ludwig-Maximilians-Universitat Munchen, and Georg-August-Universitat Gottingen. The HET is named in honor of its principal benefactors, William P. Hobby and Robert E. Eberly. The Low Resolution Spectrograph 2 (LRS2) was developed and funded by the University of Texas at Austin McDonald Observatory and Department of Astronomy, and by Pennsylvania State University. We thank the Leibniz-Institut fur Astrophysik Potsdam (AIP) and the Institut fur Astrophysik Goettingen (IAG) for their contributions to the construction of the integral field units. The authors are grateful to the HET Resident Astronomers and staff members at McDonald Observatory and Las Cumbres Observatory for their excellent work.

Facilities: RC80 (Konkoly), BRC80 (U Szeged), HET (McDonald), Las Cumbres Observatory telescopes.

Software: SALT3 (Taylor et al. 2023); MLCS2k2 (Jha et al. 2007); sncosmo (Barbary et al. 2016); Minim (Chatzopoulos et al. 2013).

Appendix

In Figures 16–19 we present plots of the bolometric LCs together with their best-fitting Arnett-models.

More plots and tables can be found online in the GitHub repository of this paper: https://github.com/borazso/PiszkeSN.

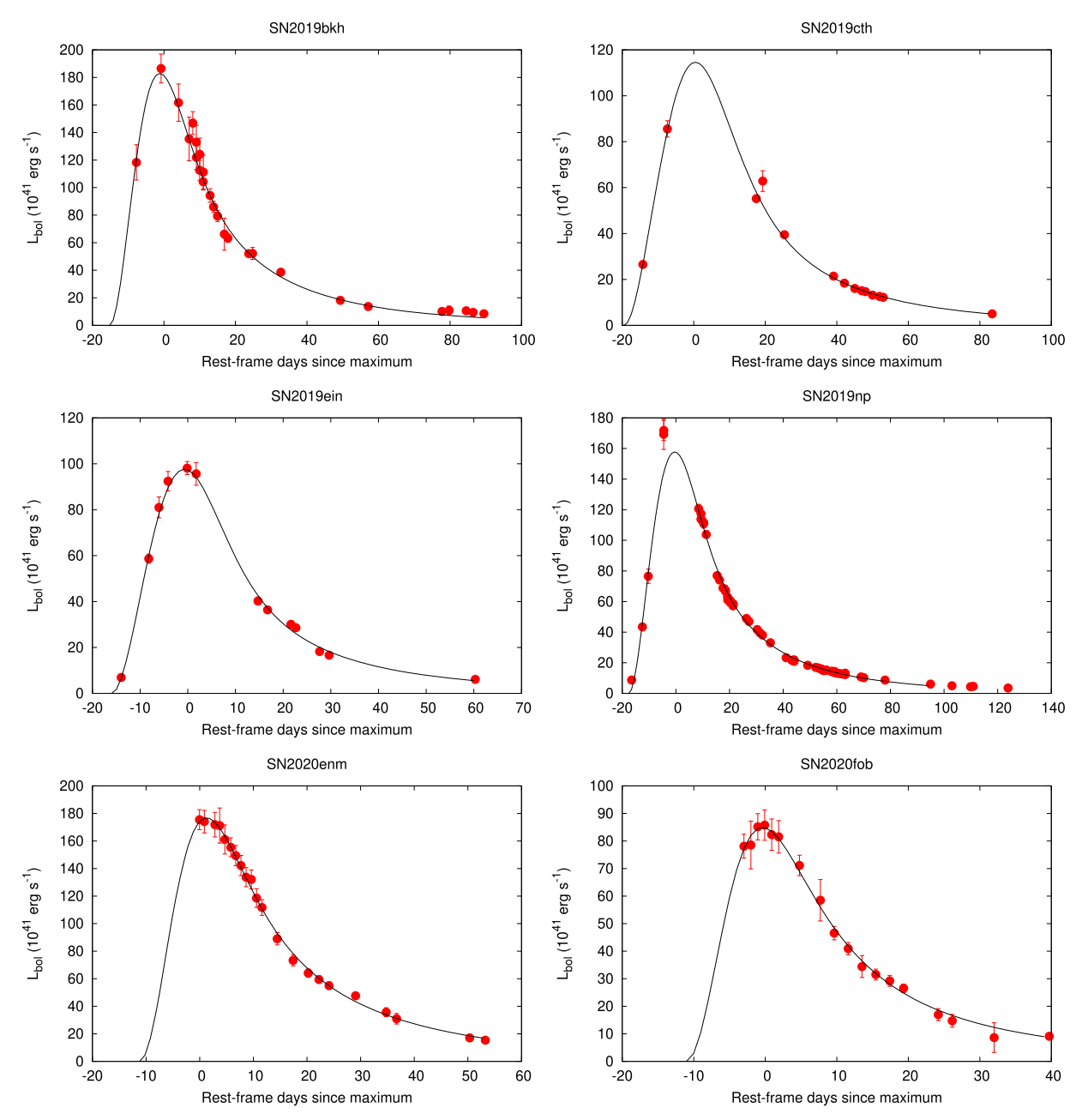


Figure 16. Bolometric light curves of the sample SNe (filled symbols) and their best-fitting Arnett-models (black curves).

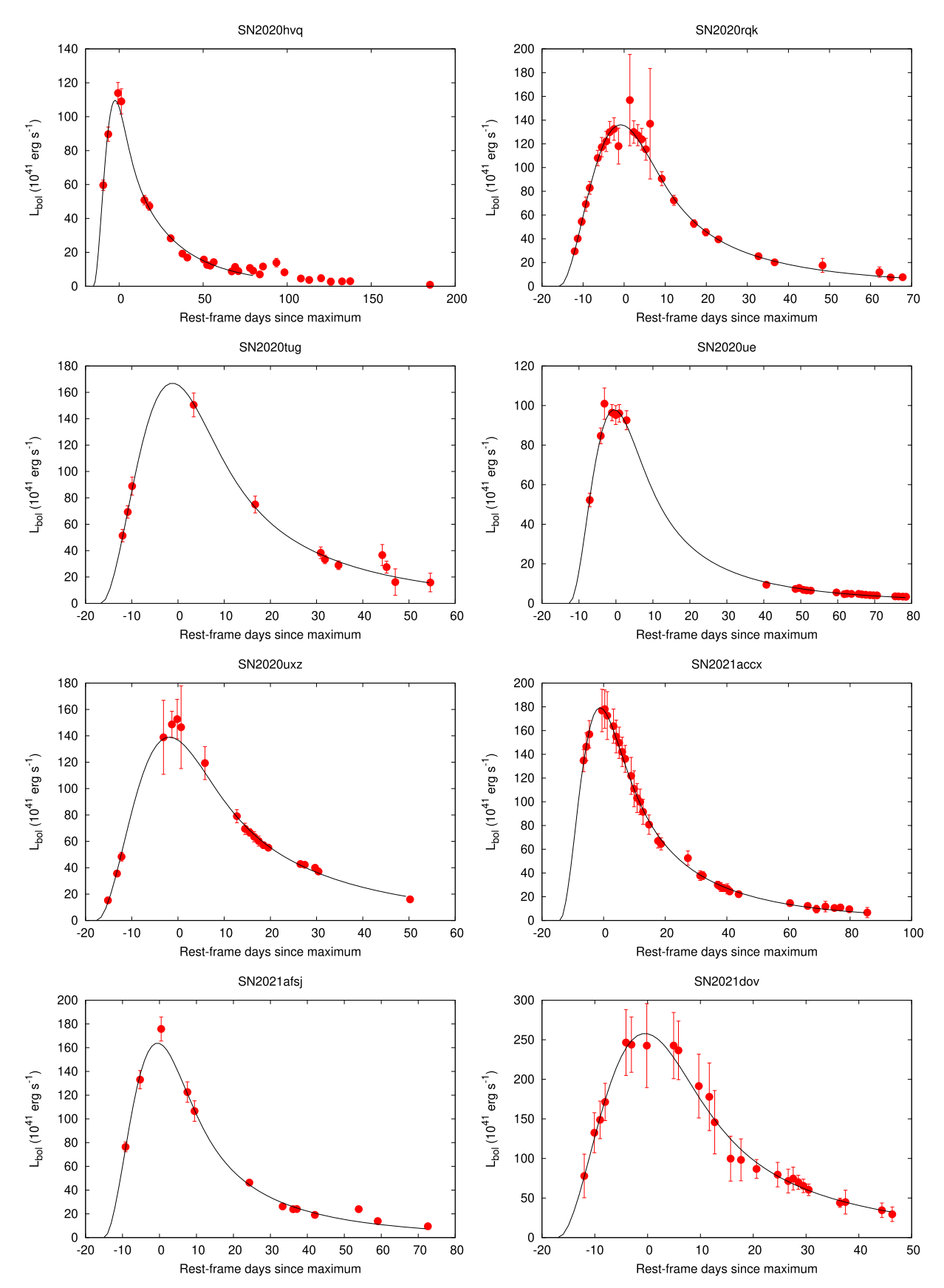


Figure 17. The same as Figure 16 but for additional SNe.

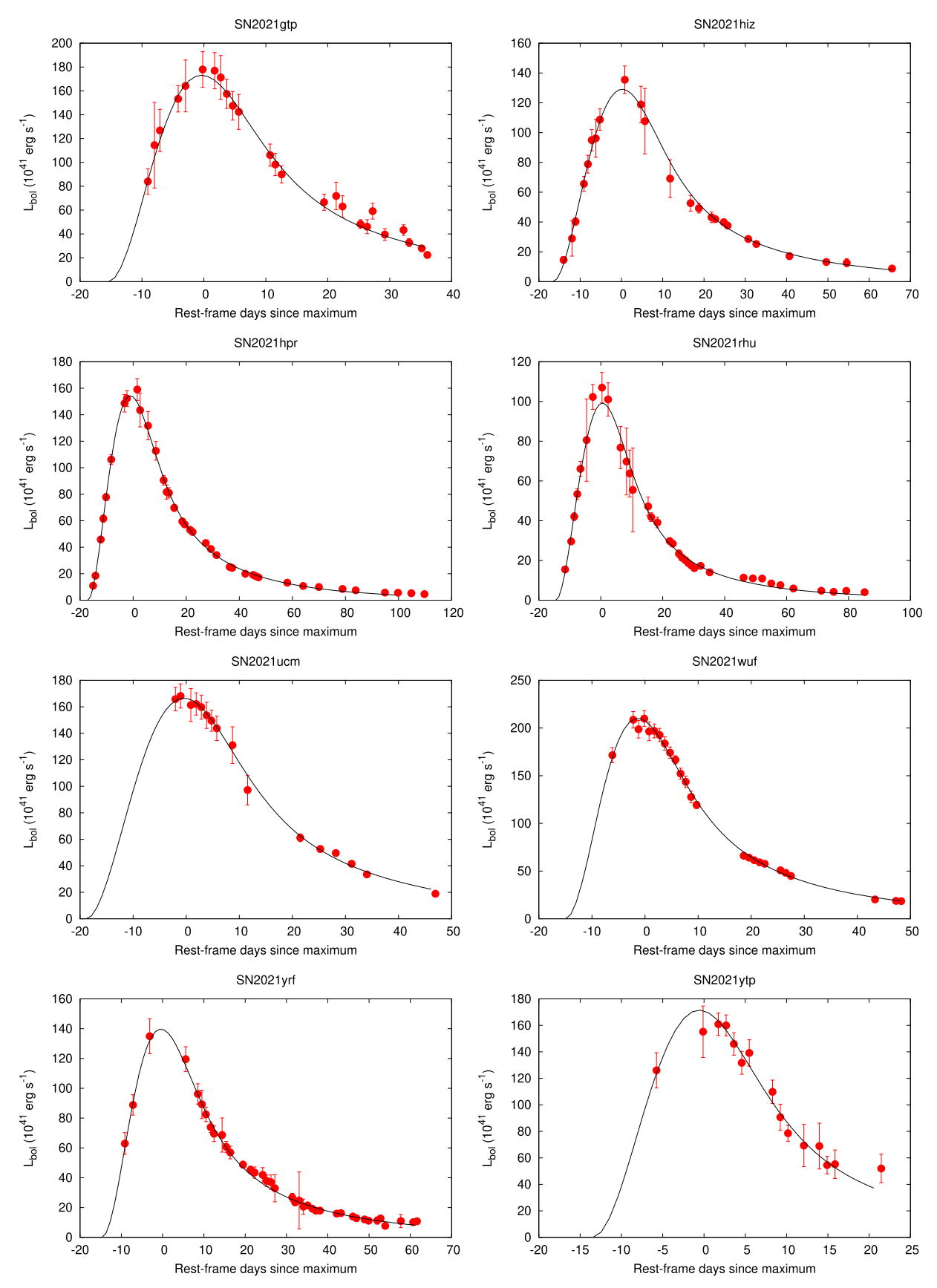


Figure 18. The same as Figure 16 but for additional SNe.

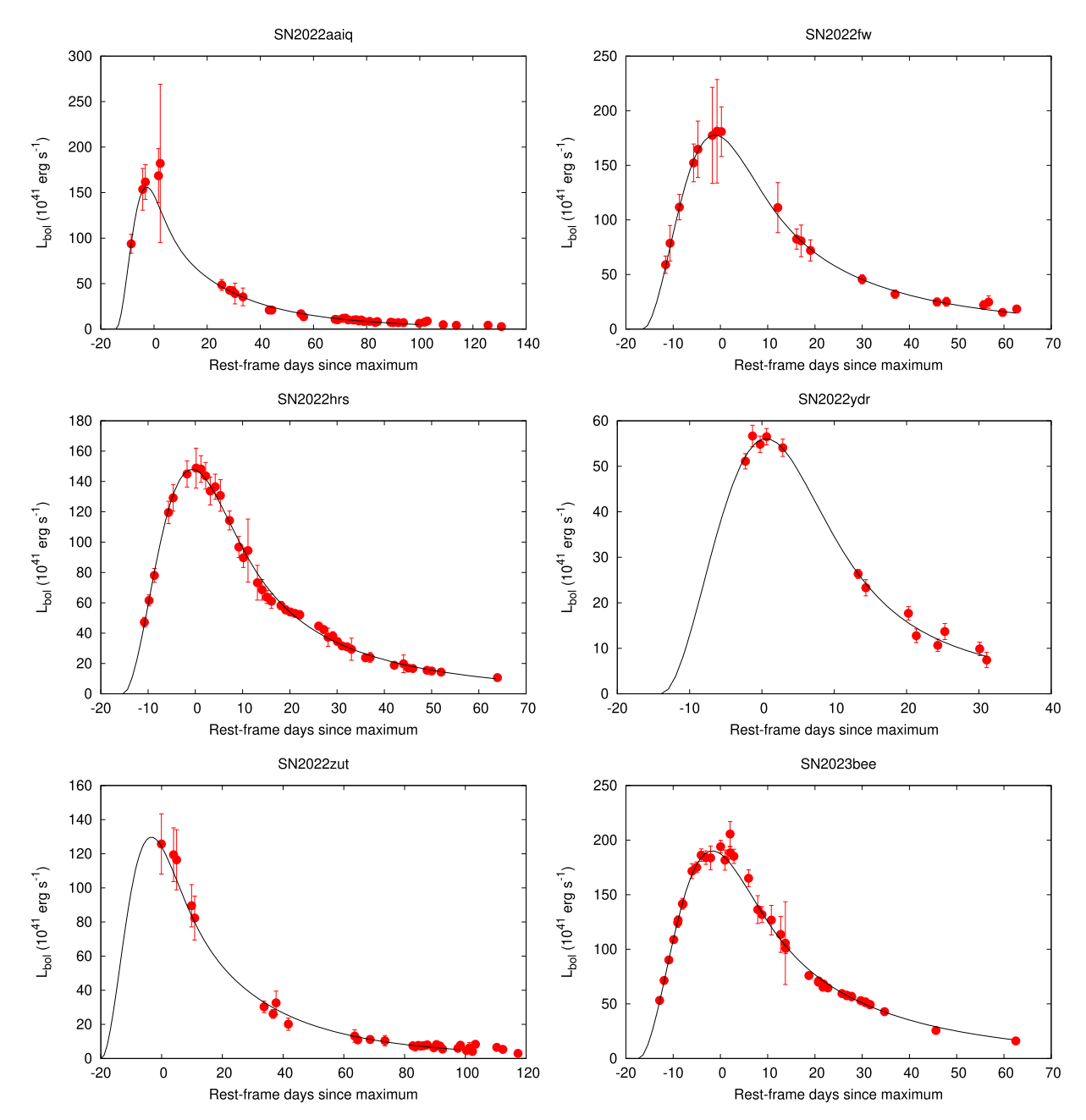


Figure 19. The same as Figure 16 but for additional SNe.

ORCID iDs

Zsófia Bora https://orcid.org/0000-0001-6232-9352 Réka Könyves-Tóth https://orcid.org/0000-0002-8770-6764

József Vinkó https://orcid.org/0000-0001-8764-7832 Imre Barna Bíró https://orcid.org/0000-0001-9061-2147 K. Azalee Bostroem https://orcid.org/0000-0002-4924-444X

Attila Bódi https://orcid.org/0000-0002-8585-4544

Borbála Cseh https://orcid.org/0000-0002-6497-8863

Joseph Farah https://orcid.org/0000-0003-4914-5625

Alexei V. Filippenko https://orcid.org/0000-0003-3460-0103

Daichi Hiramatsu https://orcid.org/0000-0002-1125-9187

D. Andrew Howell https://orcid.org/0000-0003-4253-656X

Saurabh W. Jha https://orcid.org/0000-0001-8738-6011

Csilla Kalup https://orcid.org/0000-0002-1663-0707

Máté Krezinger https://orcid.org/0000-0002-8813-4884

```
Megan Newsome https://orcid.org/0000-0001-9570-0584
Estefania Padilla Gonzalez https://orcid.org/0000-0003-0209-9246
András Pál https://orcid.org/0000-0001-5449-2467
Craig Pellegrino https://orcid.org/0000-0002-7472-1279
Bálint Seli https://orcid.org/0000-0002-3658-2175
Ádám Sódor https://orcid.org/0000-0001-7806-2883
Róbert Szakáts https://orcid.org/0000-0002-1698-605X
Tamás Szalai https://orcid.org/0000-0003-4610-1117
Giacomo Terreran https://orcid.org/0000-0003-0794-5982
Krisztián Vida https://orcid.org/0000-0002-6471-8607
```

Curtis McCully https://orcid.org/0000-0001-5807-7893

```
Xiaofeng Wang https://orcid.org/0000-0002-7334-2357
J. Craig Wheeler https://orcid.org/0000-0003-1349-6538
                             References
Arnett, W. D. 1982, ApJ, 253, 785
Atapin, K., Dodin, A., Tatarnikov, A., et al. 2021, ALeRCE Transient
   Classification Report for 2021-07-02 2021-2286, TNS
Balcon, C. 2020, Transient Classification Report for 2020-04-23
                                                                    2020-
   1113, TNS
Balcon, C. 2021, Transient Classification Report for 2021-12-01
                                                                    2021-
   4075, TNS
Balcon, C. 2022a, Transient Classification Report for 2022-04-16 2022-
   997, TNS
Balcon, C. 2022b, Transient Classification Report for 2022-10-27
   3133, TNS
Balcon, C. 2022c, Transient Classification Report for 2022-12-12 2022-
   3577. TNS
Barbary, K., Barclay, T., Biswas, R., et al. 2016, SNCosmo: Python library for
   supernova cosmology ascl:1611.017
Barna, B., Nagy, A. P., Bora, Z., et al. 2023, A&A, 677, A183
Bellm, E. C., Kulkarni, S. R., Graham, M. J., et al. 2019, PASP, 131, 018002
Benetti, S., Cappellaro, E., Mazzali, P. A., et al. 2005, ApJ, 623, 1011
Betoule, M., Kessler, R., Guy, J., et al. 2014, A&A, 568, A22
Blondin, S., Dessart, L., Hillier, D. J., & Khokhlov, A. M. 2017, MNRAS,
Bora, Z., Vinkó, J., & Könyves-Tóth, R. 2022, PASP, 134, 054201
Branch, D., Dang, L., Hall, N., et al. 2006, PASP, 118, 560
Branch, D., Dang, L. C., & Baron, E. 2009, PASP, 121, 238
Branch, D., & Wheeler, J. C. 2017, Supernova Explosions: Astronomy and
   Astrophysics Library (Berlin: Springer)
Brout, D., Scolnic, D., Kessler, R., et al. 2019, ApJ, 874, 150
Burke, J., Arcavi, I., Hiramatsu, D., et al. 2019a, Global SN Project Transient
   Classification Report for 2019-01-10 2019-71, TNS
Burke, J., Arcavi, I., Howell, D. A., et al. 2019b, Global SN Project Transient
   Classification Report for 2019-05-03 2019-701, TNS
Burke, J., Sand, D., Hiramatsu, D., et al. 2020, Global SN Project Transient
   Classification Report for 2020-10-05 2020-3032, TNS
Chatzopoulos, E., Wheeler, J. C., Vinko, J., Horvath, Z. L., & Nagy, A. 2013,
Chonis, T. S., Hill, G. J., Lee, H., et al. 2016, Proc. SPIE, 9908, 99084C
Colgate, S. A., Petschek, A. G., & Kriese, J. T. 1980, ApJL, 237, L81
Dahiwale, A., & Fremling, C. 2020a, ZTF Transient Classification Report for
   2020-02-22 2020-1504, TNS
Dahiwale, A., & Fremling, C. 2020b, ZTF Transient Classification Report for
   2020-03-31 2020-927, TNS
Dahiwale, A., & Fremling, C. 2020c, ZTF Transient Classification Report for
   2020-04-23 2020-1522, TNS
Dahiwale, A., & Fremling, C. 2021, ZTF Transient Classification Report for
   2021-03-22 2021-885, TNS
Deckers, M., Dimitriadis, G., Harvey, L., et al. 2021, ePESSTO+ Transient
   Classification Report for 2021-09-15 2021-3198, TNS
Dhawan, S., Flörs, A., Leibundgut, B., et al. 2018, A&A, 619, A102
```

```
Diamond, T. R., Hoeflich, P., Hsiao, E. Y., et al. 2018, ApJ, 861, 119
Dimitriadis, G., Siebert, M. R., Rojas-Bravo, C., et al. 2021, ATel, 14500
Du, P. L. 2020, Transient Classification Report for 2020-04-16 2020-
   1519, TNS
Fink, M., Röpke, F. K., Hillebrandt, W., et al. 2010, A&A, 514, A53
Fiore, A., Schuldt, S., Vogl, C., et al. 2019, Padova-Asiago Transient
   Classification Report for 2019-03-05 2019-2772, TNS
Flewelling, H. A., Magnier, E. A., Chambers, K. C., et al. 2020, ApJS, 251, 7
Floers, A., Taubenberger, S., Vogl, C., et al. 2020, adH0cc Transient
   Classification Report for 2020-09-22 2020-2901, TNS
Flörs, A., Spyromilio, J., Maguire, K., et al. 2018, A&A, 620, A200
Flörs, A., Spyromilio, J., Taubenberger, S., et al. 2020, MNRAS, 491,
Fremling, C., Dugas, A., & Sharma, Y. 2019a, ZTF Transient Classification
   Report for 2019-03-05 2019-2773, TNS
Fremling, C., Dugas, A., & Sharma, Y. 2019b, ZTF Transient Classification
   Report for 2019-05-10 2019-2803, TNS
Gronow, S., Côté, B., Lach, F., et al. 2021, A&A, 656, A94
Grzegorzek, J. 2021a, PSH Transient Classification Report for 2021-03-24
   2021-912, TNS
Grzegorzek, J. 2021b, PSH Transient Classification Report for 2021-04-21
   2021-1307, TNS
Grzegorzek, J. 2022, PSH Transient Classification Report for 2022-04-22
   2022-1041, TNS
Guttman, O., Shenhar, B., Sarkar, A., et al. 2024, MNRAS, 533, 994
Guy, J., Astier, P., Nobili, S., et al. 2005, A&A, 443, 781
Guy, J., Astier, P., Baumont, S., et al. 2007, A&A, 466, 11
Guy, J., Sullivan, M., Conley, A., et al. 2010, A&A, 523, A7
Harvey, L., Maguire, K., Magee, M. R., et al. 2023, MNRAS, 522, 4444
Hoeflich, P. 2017, in Handbook of Supernovae, ed. A. Alsabti & P. Murdin
   (Cham: Springer), 1151
Hosseinzadeh, G., Bostroem, K. A., Sand, D. J., et al. 2022, Global SN Project
   Transient Classification Report for 2022-01-10 2022-86, TNS
Hosseinzadeh, G., Newsome, M., Sand, D. J., et al. 2023, Global SN Project
   Transient Classification Report for 2023-02-03 2023-277, TNS
Hosseinzadeh, G., Sand, D. J., Sarbadhicary, S. K., et al. 2023, ApJL, 953, L15
Huber, M. E. 2021, SCAT Transient Classification Report for 2021-08-25
   2021-2928, TNS
Ihanec, N., Gromadzki, M., Cartier, R., et al. 2021, ePESSTO+ Transient
   Classification Report for 2021-10-28 2021-3674, TNS
Jaeger, T. D. 2021, SCAT Transient Classification Report for 2021-08-02
   2021-2660, TNS
Jha, S., Riess, A. G., & Kirshner, R. P. 2007, ApJ, 659, 122
Kasen, D. 2010, ApJ, 708, 1025
Kawabata, M., Maeda, K., Yamanaka, M., et al. 2020, ApJ, 893, 143
Kenworthy, W. D., Jones, D. O., Dai, M., et al. 2021, ApJ, 923, 265
Kessler, R., Brout, D., D'Andrea, C. B., et al. 2019, MNRAS, 485, 1171
Khatami, D. K., & Kasen, D. N. 2019, ApJ, 878, 56
Konyves-Toth, R., Vinko, J., Ordasi, A., et al. 2020, ApJ, 892, 121
Leadbeater, R. 2021, Transient Classification Report for 2021-04-04 2021-
   1048, TNS
Li, W., Wang, X., Vinkó, J., et al. 2019, ApJ, 870, 12
Li, Z., Zhang, T., Wang, X., et al. 2022, ApJ, 927, 142
Lim, G., Im, M., Paek, G. S. H., et al. 2023, ApJ, 949, 33
Liu, Z.-W., Ropke, F. K., & Han, Z. 2023, RAA, 23, 082001
Liu, J., Wang, X., Filippenko, A. V., et al. 2023b, MNRAS, 526, 1268
Livio, M., & Mazzali, P. 2018, PhR, 736, 1
Livio, M., & Riess, A. G. 2003, ApJL, 594, L93
Magee, M. R., & Maguire, K. 2020, A&A, 642, A189
Magee, M. R., Maguire, K., Kotak, R., et al. 2020, A&A, 634, A37
Maguire, K., Sim, S. A., Shingles, L., et al. 2018, MNRAS, 477, 3567
Maoz, D., Mannucci, F., & Nelemans, G. 2014, ARA&A, 52, 107
Pakmor, R., Kromer, M., Taubenberger, S., et al. 2012, ApJL, 747, L10
Pakmor, R., Kromer, M., Taubenberger, S., et al. 2013, ApJL, 770, L8
Pellegrino, C., Howell, D. A., Sarbadhicary, S. K., et al. 2020, ApJ, 897, 159
Pereira, R., Thomas, R. C., Aldering, G., et al. 2013, A&A, 554, A27
Perley, D. 2021, ZTF Transient Classification Report for 2021-04-04 2021-
   1051. TNS
Perez-Fournon, I., Poidevin, F., Angel, C. J., et al. 2022, SGLF Transient
   Classification Report for 2022-11-10 2022-3268, TNS
```

```
Pessi, P. J., Gromadski, M., & Strotjohann, N. L. 2021, ePESSTO+ Transient
   Classification Report for 2021-08-02 2021-2659, TNS
Pierel, J. D. R., Jones, D. O., Kenworthy, W. D., et al. 2022, ApJ, 939, 11
Polin, A., Nugent, P., & Kasen, D. 2019, ApJ, 873, 84
Ramirez, M., Pignata, G., Reguitti, A., et al. 2022, ePESSTO+ Transient
   Classification Report for 2022-01-11 2022-96, TNS
Riess, A. G., Press, W. H., & Kirshner, R. P. 1995, ApJI, 438, L17
Riess, A. G., Press, W. H., & Kirshner, R. P. 1996, ApJ, 473, 88
Riess, A. G., Yuan, W., Macri, L. M., et al. 2022, ApJL, 934, L7
Risin, S., Jacobus, C., Altunin, I., et al. 2023, RNAAS, 7, 229
Sai, H., Wang, X., Elias-Rosa, N., et al. 2022, MNRAS, 514, 3541
Scalzo, R., Aldering, G., Antilogus, P., et al. 2012, ApJ, 757, 12
Scalzo, R., Aldering, G., Antilogus, P., et al. 2014a, MNRAS, 440, 1498
Scalzo, R. A., Aldering, G., Antilogus, P., et al. 2010, ApJ, 713, 1073
Scalzo, R. A., Parent, E., Burns, C., et al. 2019, MNRAS, 483, 628
Scalzo, R. A., Ruiter, A. J., & Sim, S. A. 2014b, MNRAS, 445, 2535
Schlafly, E. F., & Finkbeiner, D. P. 2011, ApJ, 737, 103
Schlegel, D. J., Finkbeiner, D. P., & Davis, M. 1998, ApJ, 500, 525
Seitenzahl, I. R., Ciaraldi-Schoolmann, F., Röpke, F. K., et al. 2013, MNRAS,
   429, 1156
Shen, K. J., Kasen, D., Miles, B. J., et al. 2018, ApJ, 854, 52
Siebert, M. R., Davis, K. W., Foley, R. J., et al. 2022, UCSC Transient
Classification Report for 2022-11-17 2022-3347, TNS
SNIascore 2021, ZTF Transient Classification Report for 2021-07-05 2021-
   2331, TNS
Srivastav, S., Smartt, S. J., Fulton, M., et al. 2021, Transient Classification
```

Report for 2021-09-12 2021-3159, TNS

```
Stritzinger, M. D., Shappee, B. J., Piro, A. L., et al. 2018, ApJl, 864, L35
Sullivan, M., Kasliwal, M. M., Nugent, P. E., et al. 2011, ApJ, 732, 118
Tanikawa, A., Nomoto, K., Nakasato, N., et al. 2019, ApJ, 885, 103
Taylor, G., Jones, D. O., Popovic, B., et al. 2023, MNRAS, 520, 5209
Terwel, J. H., Maguire, K., Dimitriadis, G., et al. 2024, arXiv:2402.16962
Thompson, T. A. 2011, ApJ, 741, 82
Tonry, J. L., Stubbs, C. W., Lykke, K. R., et al. 2012, ApJ, 750, 99
Tripp, R. 1998, A&A, 331, 815
V, A., K, G., C, H., et al. 2022, Transient Classification Report for 2022-11-01
  2022-3194, TNS
Valenti, S., Sand, D., Pastorello, A., et al. 2014, MNRAS, 438, L101
Vinkó, J., Ordasi, A., Szalai, T., et al. 2018, PASP, 130, 064101
Wang, X., Filippenko, A. V., Ganeshalingam, M., et al. 2009, ApJL, 699,
  L139
Wang, X., Wang, L., Filippenko, A. V., Zhang, T., & Zhao, X. 2013, Sci,
Wheeler, J. C., Johnson, V., & Clocchiatti, A. 2015, MNRAS, 450, 1295
Wu, C., Zhang, J., Yang, Y., et al. 2019, Transient Classification Report for
  2019-01-10 2019-2765, TNS
Xi, G., Wang, X., Li, W., et al. 2022, MNRAS, 517, 4098
Yang, Y., Schulze, S., Gal-Yam, A., et al. 2020, ZTF Transient Classification
   Report for 2020-08-19 2020-2554, TNS
Zhai, Q., Zhang, J., Li, L., et al. 2023, LiONS Transient Classification Report
  for 2023-02-01 2023-260, TNS
Zhang, J., & Wang, X. 2020, Transient Classification Report for 2020-03-19
  2020-831, TNS
Zhang, Y., Zhang, T., Danzengluobu, et al. 2022, PASP, 134, 074201
```